

UC Berkeley

UC Berkeley Previously Published Works

Title

The Microscopic Mechanism of Lithiation and Delithiation in the Ag/C Buffer Layer for Anode-Free Solid-State Batteries

Permalink

<https://escholarship.org/uc/item/0436q31d>

Journal

Advanced Energy Materials, 14(10)

ISSN

1614-6832

Authors

Xie, Fengyu

Diallo, Mouhamad Said

Kim, Haegyeom

et al.

Publication Date

2024-03-01

DOI

10.1002/aenm.202302960

Copyright Information

This work is made available under the terms of a Creative Commons Attribution License, available at <https://creativecommons.org/licenses/by/4.0/>

Peer reviewed

The Microscopic Mechanism of Lithiation and Delithiation in the Ag/C Buffer Layer for Anode-Free Solid-State Batteries

Fengyu Xie, Mouhamad Said Diallo, Haegyeom Kim, Qingsong Howard Tu,*
and Gerbrand Ceder*

Lithium metal solid-state batteries (LMSSBs) have demonstrated their high energy density and cycling performance at high current densities in an anode-free architecture, featuring a thin Ag/C composite buffer layer (BL) between the current collector (CC) and the solid electrolyte (SE). This study explains the microscopic mechanism of the Ag/C BL by using first-principles atomistic and continuum modeling. It is shown that Ag effectively acts as a homogeneous solid-solution beyond $\text{AgLi}_{2.32}$ and maintains a positive potential even at AgLi_{25} during lithiation. Key factors underlying the working of the Ag/C BL include lower interfacial resistance at the BL/CC interface than at the BL/SE interface, leading to predominant Li deposition on BL/CC, and substantial Ag–Li volume expansion during lithiation. This, combined with stronger BL/SE adhesion, causes BL/SE separation and Ag–Li extrusion toward the CC side. During delithiation, Ag re-precipitates as nanoparticles uniformly on the CC, with its positive lithiation potential homogenizing Li currents in subsequent cycles. Other metals are less effective due to their relatively large overpotential, premature lithiation termination, and limited volume expansions hindering movement toward the CC. The study aids the BL design, focusing on metal choice and optimization material and microstructural properties, such as the Li-ion conductivity and interfacial resistance.

1. Introduction

Lithium-metal solid-state batteries (LMSSBs) offer a promising avenue for rechargeable battery technology due to their potential of enhanced safety and energy density.^[1–4] The use of inorganic ceramic solid electrolytes (SEs) offers non-flammability and high mechanical strength, enabling the incorporation of energy-dense Li-metal anodes, which can significantly increase the energy density of rechargeable Li-ion batteries. However, several limiting factors, such as the high costs associated with free-standing Li-metal-foil,^[5] interfacial contact loss,^[6] and unwanted (electro-)chemical reactions between the SE and Li metal,^[7] hinder the practical applications of LMSSBs. Most critically, Li-metal dendrite formation, which results from non-uniform Li-metal deposition under localized currents,^[8–10] can penetrate SEs such as oxides (including $\text{Li}_7\text{La}_3\text{Zr}_2\text{O}_{12}$, LLZO) and sulfides (including Li_3PS_4 , LPS; $\text{Li}_6\text{PS}_5\text{Cl}$, LPSCl),^[11–16] leading to battery shorting. Non-uniform Li

deposition stems from imperfect solid–solid interfaces and can be exacerbated by detrimental interphase growth^[17] and void formation^[18] during cycling.

Significant effort has been devoted to suppressing Li dendrite growth in solid-state batteries. Controlling the stack pressure^[18,19] and temperature^[20] of the solid-state cells can be beneficial in homogenizing Li deposition. Incorporating metal interlayers, such as gold (Au) and silver (Ag), also result in improvements.^[8] Recently, Lee et al.^[21] developed an Ag/C composite buffer layer (BL) and demonstrated its excellent properties in an anode-free LMSSB. In their study, $\text{LiNi}_{0.90}\text{Co}_{0.05}\text{Mn}_{0.05}\text{O}_2$ (NCM) coated with $\text{Li}_2\text{O-ZrO}_2$ was used as the cathode material and LPSCl argyrodite was used as the SE. Ag and amorphous carbon (Ag/C) were mixed into a composite film at a thickness of 5–10 μm , and the film was employed as a BL separating the current collector(CC) and SE with no Li metal used at the anode side. This “anode-less” full cell delivered an energy density of 941 Wh/L, exhibited long cycling life (89% capacity retention after 1000 cycles) and high coulombic efficiency (average > 99.8%). The excellent performance was attributed to the uniform Li deposition resulting from the use of the Ag/C BL. Several key observations should be noticed from the work of Lee et al. and follow-up work.

F. Xie, M. S. Diallo, G. Ceder
Department of Materials Science and Engineering
University of California
Berkeley, CA 94720, USA
E-mail: gceder@berkeley.edu

F. Xie, M. S. Diallo, H. Kim, G. Ceder
Materials Sciences Division
Lawrence Berkeley National Laboratory
Berkeley, CA 94720, USA

Q. H. Tu
Department of Mechanical Engineering
Rochester Institute of Technology
Rochester, NY 14623, USA
E-mail: howard.tu@rit.edu

 The ORCID identification number(s) for the author(s) of this article can be found under <https://doi.org/10.1002/aenm.202302960>

© 2024 The Authors. Advanced Energy Materials published by Wiley-VCH GmbH. This is an open access article under the terms of the [Creative Commons Attribution-NonCommercial-NoDerivs](#) License, which permits use and distribution in any medium, provided the original work is properly cited, the use is non-commercial and no modifications or adaptations are made.

DOI: 10.1002/aenm.202302960

Li-metal plating occurred at the BL-CC interface during the lithium transfer to the anode. In addition, Ag was found to move to the CC and dissolved into Li metal upon full lithiation at the anode. Upon discharge of the cell, the Li metal was stripped from the anode CC and most Ag particles did not return to the BL but remained near the CC. Through comparison with other metals (Sn, Zn, Al, and Ni), Suzuki et al.^[22] demonstrated Ag to be the best-performing metal in a metal/C BL. Later, Kim et al.^[23] proved that the Ag/C BL can also assist with homogeneous Li-metal deposition on the CC when using LLZO as the SE, with an additional layer of Ag thin film used to enhance the adhesion between the Ag/C BL and LLZO SE.

Building on the pioneering work of Lee et al.^[21] and Kim et al.,^[23] researchers have explored the thermodynamic and kinetic factors influencing uniform Li plating at the BL/CC interface. In a recent study, Park et al.^[24] demonstrated that the stronger adhesion between the BL and SE, compared to that between the BL and CC, promotes Li deposition at the BL/CC interface rather than at the BL/SE interface. Park et al. also suggested that Li migrates through the BL via Coble creep, with factors such as smaller pores and particles, higher temperatures, and lithiophilic surface modifications (e.g., Ag decoration) facilitating Li movement. In a subsequent study, Kim et al.^[25] found that the preferred plating location of Li metal is determined by the lithium-transport behavior in the BL, as evidenced by a comparative study where amorphous carbon was replaced with less Li-conductive graphite. The findings of Kim et al. align well with the observations of Suzuki et al., who noticed that Li plates between the BL and the SE when graphite is used in the BL. In contrast, when carbon black is employed in the BL, Li plating shifts to the CC side.^[22] Spencer-Jolly et al.^[26] conducted research on a Ag-graphite composite and concluded that Ag in the BL leads to relatively homogeneous Li-metal deposition between the BL and CC. However, they also found that at high current density the Ag-modified BL is not more effective in suppressing Li dendrite formation than pure graphite without Ag.

Several fundamental questions regarding the microscopic mechanism active in the Ag/C BL remain unanswered, including (1) how Ag helps homogenize current and prevent Li dendrite formation, (2) why Ag migrates to the CC side, (3) why Li only appears at the SE/CC interface, and (4) why other metals are not as effective in enhancing the cycling performance in the BL as compared to Ag. In this paper we take a multi length-scale and multi physics approach, combining ab-initio thermodynamics of Ag–Li with continuum transport and mechanics, in order to understand the role Ag plays in assisting the Li plating.

Understanding the phase stability in the Ag–Li system is critical to correctly predict the behavior of Ag during lithiation. However, the commonly used Ag–Li phase diagram is based on very limited and often outdated experimental and computational data. Pastorello^[27,28] first determined the Ag–Li phase diagram in the 1930s, reporting two intermetallic compounds: AgLi and AgLi₃. In the 1950s, a more comprehensive report by Freeth and Raynor^[29] (Figure 1a) disputed the existence of AgLi₃ and instead proposed six phases at room temperature (Figure 1b): the FCC Ag solid-solution phase ($x_{\text{Li}} = 0 - -0.46$), the β -AgLi phase with a CsCl-like structure ($x_{\text{Li}} = 0.50 - -0.56$), the $\gamma_3/\gamma_2/\gamma_1$ phases with γ -brass type structures ($x_{\text{Li}} = 0.64 - -0.93$), and the BCC Li solid-solution ($x_{\text{Li}} = 0.99 - -1.00$). Based on the

detection of two-phase coexistence at $x_{\text{Li}} \approx 0.75, 0.84$ in X-ray powder diffraction (XRD) and the presence of thermal arrests, Freeth and Raynor identified three γ phases, which they claimed to have γ -brass-like structures, informed by the observations of Perlitz.^[30] However, without any original XRD pattern or thermal measurement data provided in Freeth and Raynor's paper, the existence and structures of these γ phases, especially the γ_2 and γ_1 phases, remain unclear. More precise XRD measurements by Arnberg and Westman^[31] revealed that the γ_3 structure aligns more closely with the Cu₅Zn₈-prototype than with the Al₄Cu₉ structure type, a claim that more recent measurements^[32] have confirmed. Arnberg and Westman also attempted to synthesize γ_2 and γ_1 , but failed as Li-rich samples easily react with air. The Ag–Li phase diagram, especially on the Li-rich side, has not been significantly updated since this early work. Pelton's work in the 1980s^[33] mostly drew from the results of Freeth and Raynor,^[29] with some additional investigations into the liquidus line. Recently, Braga et al.^[34] claimed the γ_1 phase to be nonexistent by comparing the first-principles free-energy calculation results of the γ and BCC phases. Braga et al. also suggested the γ_2 phase to be a Ag₁₅Li₄₉ BCC structure instead of the Pb₃Li₁₀-like structure hypothesized by Freeth and Raynor. However, the similarity in the XRD patterns of Ag₁₅Li₄₉ and Ag₃Li₁₀ along with potential interference from impurities make the second claim difficult to verify experimentally. Furthermore, the calculations of Braga et al.^[34] in the BCC and FCC structures used only a single special quasi-random structure (SQS) at each composition^[35] to represent the energy of the solid solution without any configurational entropy to evaluate its ability to destabilize ordered compounds at non-zero temperature.

In this article, we employ first-principles thermodynamic calculations to determine the free energy of each phase in the Ag–Li alloy system, incorporating the electronic energy, configurational entropy, and phonon free energy. The phase stability and lithiation voltage into Ag are analyzed using the computed free energy. Continuum modeling is applied to study the Li transport in a Ag–C buffer layer (BL), the current density distribution in the BL and at interfaces, and the mechanical behavior during lithiation and delithiation, as well as to analyze the migration of Ag particles. By integrating results from various models, we provide a comprehensive explanation of the microscopic mechanism during the cycling of a Ag/C BL and suggest optimal BL metal choices and processing conditions.

2. Results and Discussion

2.1. Approach

We systematically investigated the phase stability in the Ag–Li system using first-principles calculations to determine low-energy Ag–Li configurations on multiple possible lattices. We iteratively searched for ground-state configurations,^[36] covering the FCC Ag solid-solution phase and BCC-derived phases (β -AgLi and BCC Li solid-solution) at $x_{\text{Li}} = 0 - -1$ (Figure 1b).

As shown in Figure 1c, the γ -brass crystal structure resembles the BCC crystal structure. The γ -brass structure can be obtained from a BCC 3*3*3 supercell by removing the corner and center atoms and relaxing the remaining atoms under the symmetry

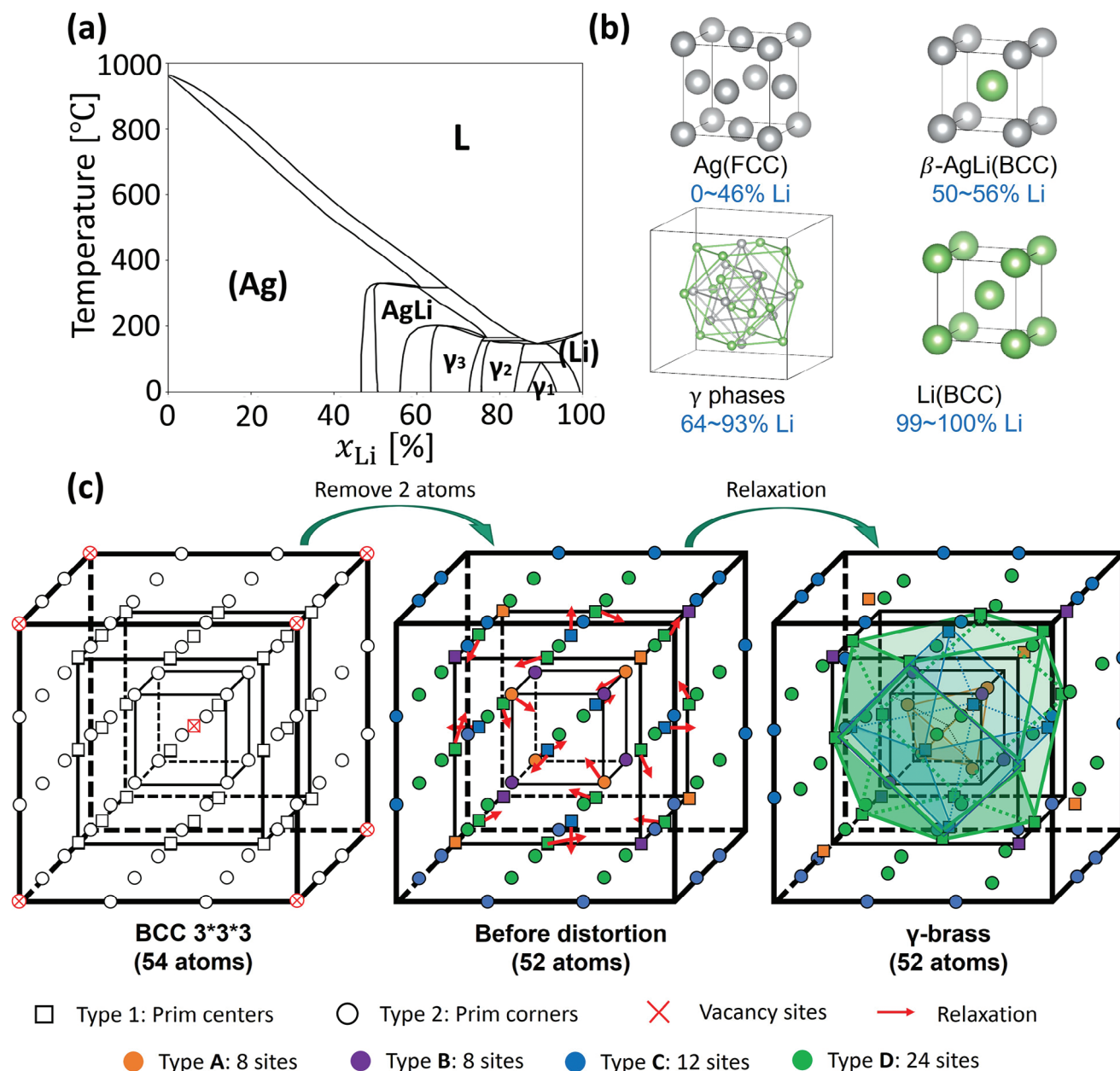


Figure 1. a) Experimental temperature–composition phase diagram of the Ag–Li system, redrawn from the data of Freeth and Raynor.^[29] b) Crystal structure of phases in the Ag–Li system at room temperature, including (Ag), β -AgLi, γ -brass phases, and (Li). c) The γ -brass structure and its relationship to the BCC structure. The left subplot shows a $3 \times 3 \times 3$ supercell containing 54 atoms, scaled from the conventional BCC cubic cell. Atoms located at the body centers of the conventional cube are marked as type 1 (squares), whereas atoms located at the body corners are marked as type 2 (circles). The middle subplot shows the supercell with 52 atoms remaining after removing two atoms at the center and corners of the supercell (red cross). The remaining sites are grouped into four sub-lattices: type A (orange), type B (purple), type C (blue), and type D (green). For visibility, only the relaxing direction of the A_2 , B_2 , C_1 , and D_1 atoms are marked in red arrows. The relaxing direction of the other atoms can be found by applying symmetry in the $\bar{I}43m$ space group. The right subplot shows the resulting γ -brass structure after relaxation. Polygon clusters formed by atoms on different sub-lattices are marked and shaded with the corresponding colors of their sub-lattices.

of the $\bar{I}43m$ space group. Atoms in the γ -brass structure can be grouped into four symmetrically distinct sub-lattices:^[37]

1. Type A (orange): eight sites, forming the innermost tetrahedral cluster around vacancies;
2. Type B (purple): eight sites, forming a larger tetrahedral cluster outside the cluster of A;
3. Type C (blue): 12 sites, forming an octahedral cluster outside the cluster of A and B;
4. Type D (green): 24 sites, forming the largest cluster encapsulating the clusters of A, B, and C.

Table 1. Experimentally observed prototypes of γ -brass structures, extracted from the Materials Project and the ICSD database. F&R represents Freeth and Raynor.^[29]

Prototype	Ag/Li occupancy	Refs.	Notes
Cu ₅ Zn ₈	A, D: Li; B, C: Ag/Li mixed	[41]	Experimentally confirmed γ_3 ;
Al ₄ Cu ₉	A ₂ , D ₁ (or A ₁ , D ₂): Ag; Other: Li	[42]	Proposed by F&R as γ_3 .
Pb ₃ Li ₁₀	D ₂ (or D ₁): Ag; Other: Li	[43]	Proposed by F&R as γ_2 .
RuAl ₁₂	A ₁ (or A ₂): Ag; Other: Li	[44]	Proposed by F&R as γ_1 .
Fe ₄ Zn ₉	A: Ag; C: Ag/Li=2:1; B, D: Li	[45]	DFT assumed all C sites to be occupied by Ag, giving $x_{Li} = 8/13$.
In ₅ Ti ₈	A ₁ , B ₁ , D ₁ (or A ₂ , B ₂ , D ₂): Ag; Other: Li	[46]	

Different γ -type structures differ by the distribution of the components over these sites. In other studies,^[32,38] types A, B, C, and D are also denoted as IT, OT, OH, and CO, respectively. Each sub-lattice can be further divided based on symmetry breaking of the original positions in the BCC lattice: type 1 (squares) for sites originally on the cubic centers and type 2 (circles) for sites originally on the cubic corners. In Table 1, structural data from the Materials Project^[39] and the ICSD database^[40] are used to classify all experimentally observed γ -brass structures into six distinct prototype classes with different sub-lattice occupancies. We used these as a starting point to evaluate possible γ -brass type phases in the Ag–Li system. Under the Cu₅Zn₈ prototype, we enumerated Ag–Li configurations from $x_{Li} = 8/13$ to $x_{Li} = 1$, assuming that Ag can only be located at B and C sites with further DFT computations performed on all five other γ -brass prototypes (as shown in Table 1) to validate the assumption on Ag occupancy limitation.

To capture the free energy of Ag–Li phases, we fit cluster-expansion (CE) models for BCC, FCC, and γ (exclusively Cu₅Zn₈ prototype) lattices. A cluster expansion^[47,48] is a well-established approach in ab initio alloy theory to parameterize the configurational energy dependence so that it can be sampled with Monte-Carlo (MC) techniques.^[49] We performed MC simulation at varied temperatures (T) and Li contents (x_{Li}) and integrated the sampled energy over temperatures to obtain the configurational free energy. The configurational free energy values are interpolated over compositions using a B-Spline fit to represent the free energy as a continuous function of composition. We accounted for lattice vibrations by adding phonon free energy into the CE-MC result. Details about these methods can be found in the Experimental Section.

The transport behavior of Ag and Li in the BL was investigated with electro-chemo-mechanical modeling. We described the conduction of Li-ions and electrons in the BL by applying mixed ionic-electron conducting theory,^[50] modeled the redox reaction of Li at the SE/BL and CC/BL interfaces with the Butler–Volmer relation,^[7] simulated the diffusion of Li and Ag in the alloy using the Cahn–Hilliard equation,^[51] and investigated the plastic flow of Li in BL with elastoplastic mechanics.^[52] Key parameters that govern Li deposition at the BL/CC interface and the Ag migration toward CC were systematically examined. These factors include the area-specific charge transfer resistance (ASR), the adhesive strength at different interfaces, the lithiation potential in the Ag particles, and the pressure developed within the BL. We also investigated the factors that affect the Li-current distribution on the CC surface, aiming to understand the role of Ag in homogenizing Li deposition and provide strategies for optimized anode-free bat-

tery design. More detailed explanations about these simulations are provided in the Experimental Section. All the relevant partial differential equations were solved with self-developed programs based on the Finite Element Method.^[53] Parameters used in these simulations can be found in the Supporting Information.

2.2. Results

2.2.1. Phase Stability in the Ag–Li System

Figure 2 presents the zero-K formation energy of each structure enumerated within BCC, FCC, Cu₅Zn₈- γ lattice models, along with the other five γ prototypes shown in Table 1. The energy of FCC Ag and BCC Li were used as references. As shown in Figure 2a, the ground-state configurations on BCC and FCC lattices at $x_{Li} = 0.5$ were found to be a Pm3m CsCl-type cubic structure (indicated by a red arrow) and an I4₁/amd tetragonal structure (indicated by a green arrow), respectively. The energy of the Pm3m cubic structure is 5.2 meV/atom below the I4₁/amd structure. The ground state at $x_{Li} = 0.75$ appears to be a BCC AgLi₃ structure (Figure 2b) with DO₃ ordering (i.e.,

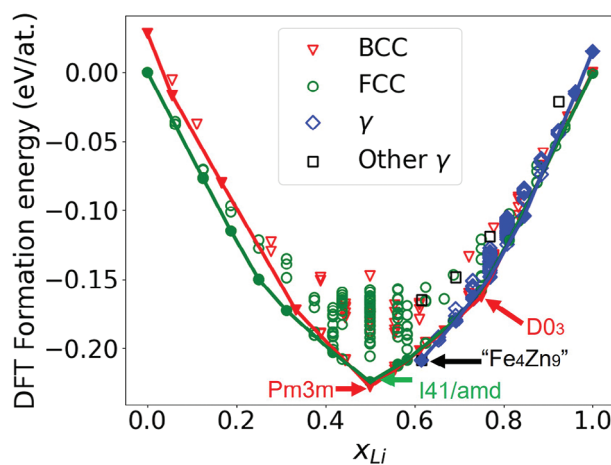


Figure 2. DFT computed zero-K formation energy of Ag–Li structures in BCC (red triangles), FCC (green circles), Cu₅Zn₈ γ -brass (blue diamonds), and other γ prototypes (black squares). Convex hulls are shown for all compounds within a structural type, with structures on the convex hulls marked by solid markers. The formation energy of the FCC I4₁/amd structure, BCC Pm3m structure at $x_{Li} = 0.5$, and BCC DO₃ structure at $x_{Li} = 0.75$ are marked with arrows.

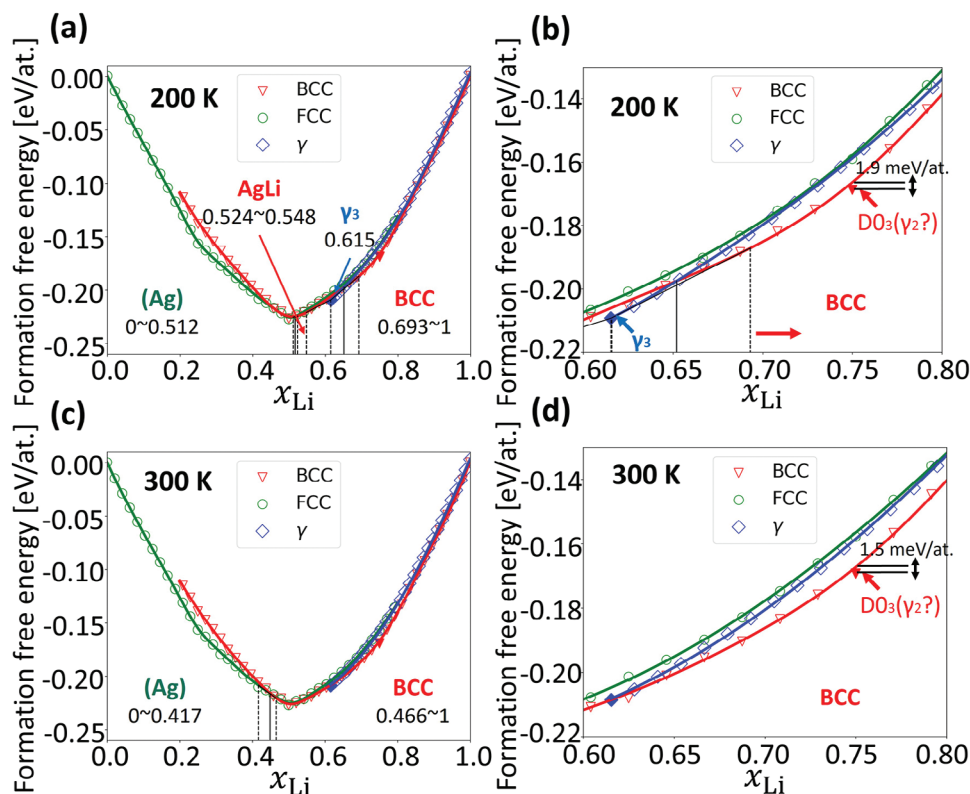


Figure 3. Formation free energy of Ag–Li BCC (red), FCC (green), and γ (blue) phases as a function of Li content (x_{Li}) at $T=200$ K (a–b) and 300 K (c–d). (a,c) show free energy functions in the range of $x_{\text{Li}} = 0 - 1$. (b,d) show free energy functions in the range of $x_{\text{Li}} = 0.6 - 0.7$. Predicted phase boundaries are marked with black dashed lines, and the intersections between the free energy curves are marked with black solid lines.

BiF₃ ordering). All the other γ prototypes (hollow black squares) exhibit significant instability (>50 meV/atom) relative to structures belonging to the Cu₅Zn₈ prototype, with the exception of the Fe₄Zn₉-like structure that relaxes to the Cu₅Zn₈-like structure and therefore yields the same energy (hollow black square overlapping with solid blue diamond at $x_{\text{Li}} = 8/13$; refer to the [Supporting Information](#) for structural relaxation details). This high energy of other γ -prototype structures may arise from repulsive short-ranged Ag–Ag interactions occurring between A and D sites, validating our assumption that Ag should only exist on B and C sites. Thus, we should exclude other γ -brass prototypes with Ag on A and D sites, including those proposed by Freeth and Raynor.^[29]

Based on the DFT ground-state analysis, we proceed with the computation of free energy for the BCC, FCC, and γ (Cu₅Zn₈-prototype only) lattice structures. **Figure 3** shows the formation of free energy as a function of x_{Li} ($\Delta F(x)$) at $T = 200$ K and 300 K. At $T = 200$ K (Figure 3a), we identify four stable phases: the FCC Ag phase from $x_{\text{Li}} = 0$ to 0.512 , the β -AgLi phase with a CsCl-like crystal structure from $x_{\text{Li}} = 0.524$ to 0.548 , a γ -brass phase with $x_{\text{Li}} = 8/13$ stoichiometry and a BCC solid solution for $x_{\text{Li}} = 0.693 \approx 1$. Only one γ phase emerges in Figure 3a, corresponding to the γ_3 phase proposed by Freeth and Raynor.^[29] Upon increasing the temperature to $T = 300$ K (Figure 3c), BCC is stabilized over γ_3 due to both configurational and vibrational entropy effects (refer to [Supporting Information](#)). At this temperature, only the FCC Ag phase and the BCC solid solution per-

sists. The transformation of γ_3 into BCC at high temperatures agrees well with the qualitative trends seen in the experimental phase diagram (Figure 1a) though it is clear that our computations predict too low a temperature at which γ_3 transforms into BCC. It should be noted that the transformation temperature is highly sensitive to small errors in the energy or entropy differences between the structures. In Figure 3b,d, the D₀₃-AgLi₃ structure is determined to be the equilibrium structure at $x_{\text{Li}} = 0.75$, with its free energy being 1.9 and 1.5 meV/atom below the interpolated free energy of the BCC solid solution at $T = 200$ and 300 K, respectively. This could potentially indicate that D₀₃-AgLi₃ is a new phase within the BCC lattice; however, this claim may lack statistical robustness considering the magnitude of the interpolation error (≈ 1 meV/atom) and the BCC CE error (3.3 meV/atom). Further results from semi-grand canonical MC simulations on the BCC lattice can be found in the [Supporting Information](#), showing the presence of the D₀₃-AgLi₃ structure manifests in chemical potential–composition curve at $x_{\text{Li}} = 0.75$ when $T \leq 300$ K. This finding suggests that D₀₃-AgLi₃ may indeed precipitate from the disordered BCC solid solution as a new phase when $x_{\text{Li}} \approx 0.75$ and $T \approx 300$ K. The Supporting Information also features simulated XRD patterns of the BCC D₀₃-AgLi₃ structure and a representative γ -brass structure at $x_{\text{Li}} = 0.75$ drawn from MC samples. These patterns suggest a significant structural similarity between the two structures such that they might not be easy to distinguish in experiments. Therefore, it is possible that the previously reported γ_2 phase might

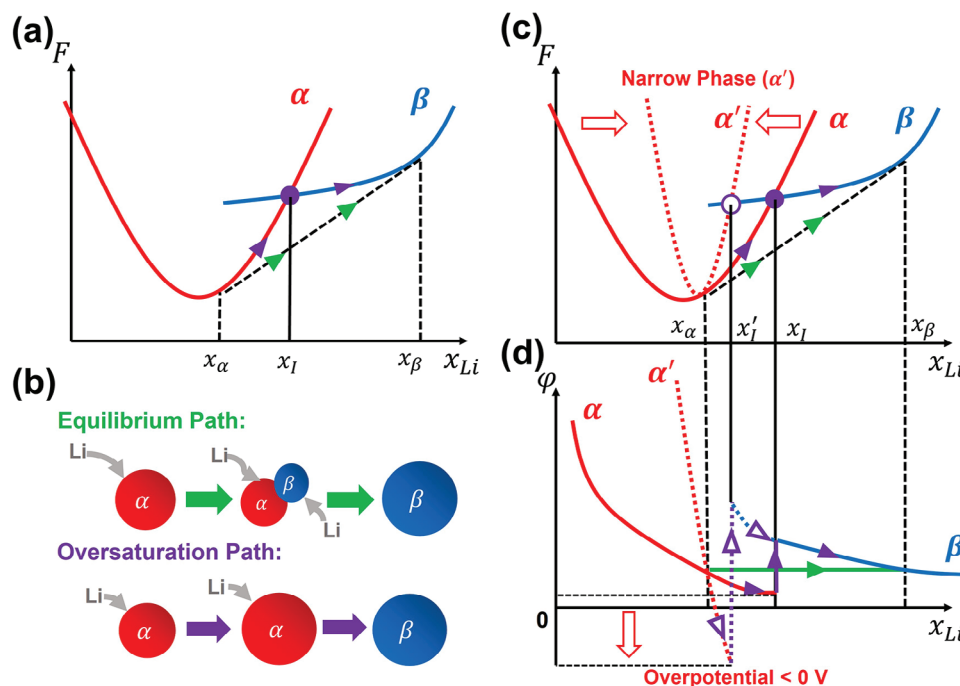


Figure 4. a) The path of metal-Li free energy (F) during lithiation when undergoing an equilibrium (green arrow) or over-saturation (purple arrow) transformation from the α phase (red curve) to the β phase (blue curve). x_α , x_β , and x_I represent the solubility limits of α , β , and the intersecting composition of α and β free energy, respectively. b) Microscopic mechanism for both the equilibrium and over-saturation transformation. c) Free-energy paths assuming that the free energy of phase α will increase more rapidly when the composition deviates from the minimum free-energy composition, with a sharper free-energy curve (α' , red dashed curve). d) Lithiation potential when comparing the original phase α and the narrowed phase α' . The overpotential of α' drops below 0 V at the intersecting composition x'_I .

in fact be BCC $D0_3$ - $AgLi_3$. The γ_1 phase described by Freeth and Raynor could potentially represent a Li solid solution as no phase transformation can be identified in our calculations for $x_{Li} > 0.85$. The free energy difference between BCC and γ -brass in Figure 3 is very small, usually less than 5 meV/atom. This similarity in energy can be rationalized by their structural similarity (Figure 1c) given that γ -brass is essentially BCC with vacancies and partial ordering. The energy similarity of BCC and γ also hints at the possibility that once Ag is lithiated over $x_{Li} \approx 0.6$, the Ag-Li system will behave practically as a BCC solid solution that retains a driving force to absorb Li, despite the fact that some γ phases can form and coexist with the BCC solid solution.^[26]

We considered both the equilibrium voltage curve derived from these free energy curves, as well as possible non-equilibrium voltage behavior through the phase transitions. The phase transformations within the Ag-Li system can be broadly classified into two types:

- Incoherent transformations: These transformations involve changes in the crystal lattice geometry, such as the transformations from FCC Ag to BCC β -AgLi, from β -AgLi to γ_3 , and from γ_3 to BCC.
- Coherent transformations: These transformations maintain the topology of the lattice while atom ordering on the lattice varies with composition. For example, the formation of $D0_3$ -AgLi₃ from BCC solid solution.

For incoherent transformations, the Ag lithiation potential can be estimated by differentiating the free energy along two distinct transformation paths, as indicated in Figure 4a,b:

1. The equilibrium path, represented with green arrows, involves phase segregation to form distinct phases separated by moving interfaces, causing the free energy of the system to follow the common tangent line in the two-phase region ($x_\alpha < x_{Li} < x_\beta$).
2. The over-saturation path, depicted by purple arrows, includes over-lithiation of Ag particles past the equilibrium composition ($x_{Li} > x_\alpha$) until the particle undergoes spontaneous transformation between phases at fixed composition, thereby avoiding the need for long-range diffusion and two phase coexistence. Such a process occurs when particle sizes are small and phase separation is energetically unfavorable due to the energy penalty of forming interfaces.^[51]

Because it can be difficult for phase transformations to occur in equilibrium at room temperature, we assume in this study that oversaturation of a phase can occur as long as the oversaturated phase has a lower free energy than the new phase that needs to form. For the example in Figure 4, phase α can be metastable up to composition x_I , which is larger than the composition x_α where the equilibrium transition would occur. Such interpretation has previously been used to understand non-equilibrium paths in other intercalation electrodes.^[54] Over-saturation reduces the potential of the alloy below the equilibrium potential and can even

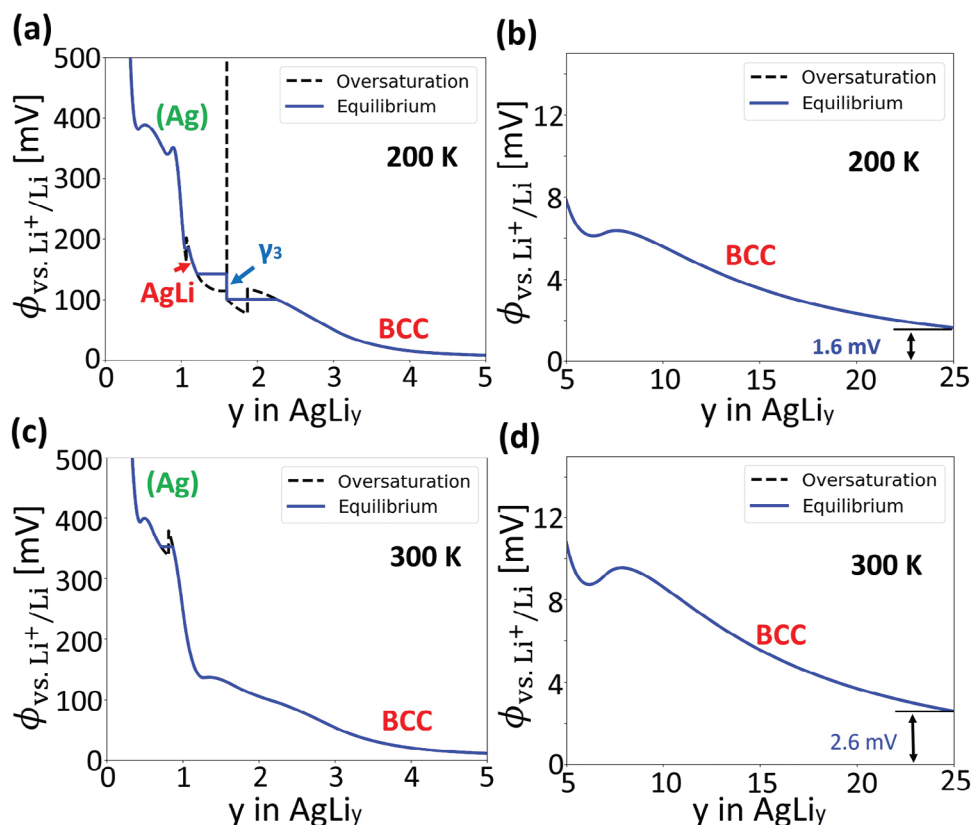


Figure 5. Computed lithiation potentials of Ag from equilibrium (blue solid) and over-saturation (black dashed) paths as functions of y in formula AgLi_y , calculated at a, b) $T=200$ K and c, d) $T=300$ K. (a, c) show the lithiation potentials in $y = 0 - 5$, and (b, d) show the lithiation potentials in $y = 5 - 25$.

bring it below 0 V. As Figure 4c,d show, when the free energy (F) of α (solid red curve) increases more rapidly away from the equilibrium composition x_{α} , resulting in a narrower curve (α' , red dashed curve), the lithiation potential (ϕ) of α' decreases more rapidly below the equilibrium potential for $x_{\text{Li}} > x_{\alpha}$, eventually reaching a minimum overpotential below 0 V. Once the lithiation potential dips below 0 V, lithiation stops within the alloy, instead causing Li-metal deposition elsewhere. Hence, in such a situation, it can be difficult to form the new phase β .

For the coherent transformation between BCC-Li and BCC $\text{DO}_3\text{-AgLi}_3$, the formation of $\text{DO}_3\text{-AgLi}_3$ can be reasonably disregarded. In situ XRD experiments^[26] suggest that the formation of $\text{DO}_3\text{-AgLi}_3$ (denoted as $\text{Ag}_3\text{Li}_{10}$ by Spencer-Jolly et al.) is slow under high charging current, with noticeable $\text{Ag}_3\text{Li}_{10}$ formation after ≈ 1 h at $2 \text{ mA}\cdot\text{cm}^{-2}$.

Figure 5 shows the Ag lithiation potential as a function of y in the formula AgLi_y at temperatures of 200 and 300 K. At these temperatures, no incoherent transformations occur that would yield a negative over-saturation potential (see Figure 5a,c), indicating that they can occur without causing Li plating reactions. As shown in Figure 5b,d, even at a high Li content ($y = 25$), Ag possesses a positive lithiation potential of 1.6 and 2.6 mV at 200 and 300 K, respectively. As a result, Ag will continue to lithiate, forming a solid solution, and the Ag-Li alloy will maintain this ability, even at very high Li content. The chemical driving force introduced by Ag is essential in rationalizing its role in equalizing Li deposition, as will be demonstrated in the Discussion section.

2.2.2. Transport of Ag and Li in the Ag/C BL

Figure 6a provides the schematics of a BL model used to investigate the dominant factors governing the transport and reactions of Ag and Li inside the BL. This model BL is comprised of a Ag particle (green) of diameter $d = 40$ nm (an average diameter estimated from the data of Lee et al.^[21]) in the center and an amorphous carbon layer (dark grey) of thickness $H = 10 \mu\text{m}$.^[21] The Li-ion conductivity of the BL is estimated to be $1 \text{ mS}\cdot\text{cm}^{-1}$.^[55] Given that carbon lithiates before silver,^[26] the amorphous carbon is assumed to be saturated already to LiC_6 and serve as a mixed ionic-electronic conductor (MIEC) due to its substantial ionic and electronic conductivity.^[56-59] It is important to note that we reference a 40% porosity in the BL, which is derived from the data provided by Lee et al.^[21] This estimation is inherently subject to the influence of the material's microstructure, the methodologies employed during pre-processing, and the external conditions such as the stacking pressure. Consequently, the actual BL could be denser than our estimations, potentially driving the true porosity well below 40%. Additionally, given the relatively small amount of Ag (constituting merely 1.6% of the BL's volume^[21]) in comparison to the BL's porosity (approximated at 40% of the BL's volume), it is likely that Ag particles might not be present within every pore. Considering that an Ag particle is only required to occupy the pore it resides in to effectively extrude, the volumetric expansion necessary prior to Ag extrusion could also be less than that required by the 40% estimation. Given these considerations,

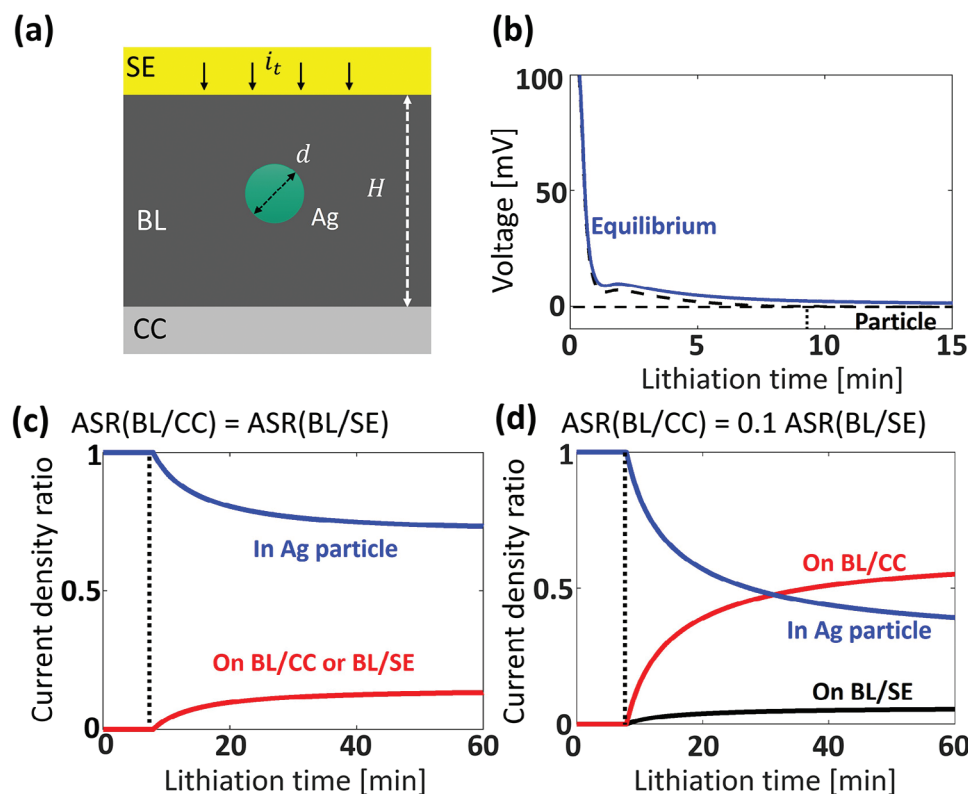


Figure 6. Continuum simulation results of a single particle in the BL under symmetric ($ASR(BL/SE) = ASR(BL/CC) = 20 \Omega \cdot \text{cm}^2$) and asymmetric interface ASRs ($ASR(BL/SE) = 20 \Omega \cdot \text{cm}^2$, $ASR(BL/CC) = 2 \Omega \cdot \text{cm}^2$). a) Simulation setup. A silver particle (green) of diameter $d = 40 \text{ nm}$ was placed within a BL (grey) of thickness $H = 10 \mu\text{m}$, and the system was lithiated under a constant current density $i_t = 0.68 \text{ mA} \cdot \text{cm}^{-2}$. The Li-ion conductivity of the BL is estimated to be $1 \text{ mS} \cdot \text{cm}^{-1}$. b) Simulated electrochemical potential of the Ag particle (black dashed) and the equilibrium bulk potential (blue solid) as functions of lithiation time. c,d) Ratio of Li current flowing into the Ag particle, depositing on the BL/CC and BL/SE interfaces as functions of lithiation time, assuming (c) equal ASRs on the BL/CC and BL/SE interfaces and (d) lower ASR on the BL/CC interface.

determining the exact volumetric expansion required for extrusion could be challenging. Thus, we employed a 40% porosity estimate for demonstrative purposes in our study, while welcoming future experimental works to accurately determine the BL's porosity. The detailed simulation parameters and their references are provided in the Supporting Information.

Continuum transport simulations were performed under constant lithiation current density of $i_t = 0.68 \text{ mA} \cdot \text{cm}^{-2}$ for two scenarios: 1) equivalent interfacial charge-transfer area-specific resistance (ASRs) at interfaces BL/SE and BL/CC of $20 \Omega \cdot \text{cm}^2$ to highlight the alloying effect from the Ag particle; 2) nonequivalent interfacial charge-transfer ASRs (BL/SE: $20 \Omega \cdot \text{cm}^2$, BL/CC: $2 \Omega \cdot \text{cm}^2$, Figure 6d), to represent a more realistic scenario as the ASR at the BL/CC interface is lower than that at the BL/SE interface.^[60,61] Figure 6b illustrates the evolution of the voltage in the Ag particle as a function of lithiation time by assuming that the Li distribution within the Ag nano-particle can be homogenized instantly. The blue curve represents the equilibrium lithiation voltage re-plotted from Figure 5a,b with the x-axis converted to lithiation time under the given charge rate. The potential of the actual Ag particle (black dashed) declines more rapidly than the equilibrium potential in the bulk alloy due to the additional overpotential required to overcome the Li-ion transport resistance in the bulk BL and the charge transfer resistance at the Ag/BL interfaces (Figure 6b). Figure 6c,d show the fraction

of Li current alloying with the Ag particle or depositing on the BL/SE and BL/CC interfaces as functions of lithiation time. In Figure 6c the ASRs for BL/SE and BL/CC are equal, whereas in Figure 6d the ASR at BL/CC interface is lower. At the beginning of lithiation, the Ag particle exhibits a positive potential, absorbing nearly all the Li. However, after $\approx 8 \text{ min}$, the Ag particle potential becomes negative (dashed lines), triggering Li deposition on the BL/SE and BL/CC interfaces. Since the electronic conductivity of the BL is very high ($\approx 10^4 \text{ mS} \cdot \text{cm}^{-1}$),^[12] the electrochemical potential of electron at the BL/SE and the BL/CC interfaces should be almost equal, causing the charge transfer resistance to be the dominating factor of Li deposition rate. When the ASRs at both interfaces are equal, Li deposits at approximately equal rates on the BL/SE and BL/CC interfaces, as shown in Figure 6c. However, studies^[21,22,60,61] suggest that the ASR at the BL/CC interface is usually lower than that at the BL/SE interface, causing the CC side to attract a larger portion of Li current as is evident in Figure 6d.

As lithiation continues, the Ag–Li alloy expands within the pores of the BL and densifies it. According to the research of Lee et al.,^[21,22] Ag particles initially constitute roughly 2% of the total volume in the BL, which possesses an initial porosity of approximately 40%. We used these values to plot in Figure 7a the relative volume percentage the Ag–Li will take up in the BL as a function of time at a charge rate of $0.68 \text{ mA} \cdot \text{cm}^{-2}$. The volumes

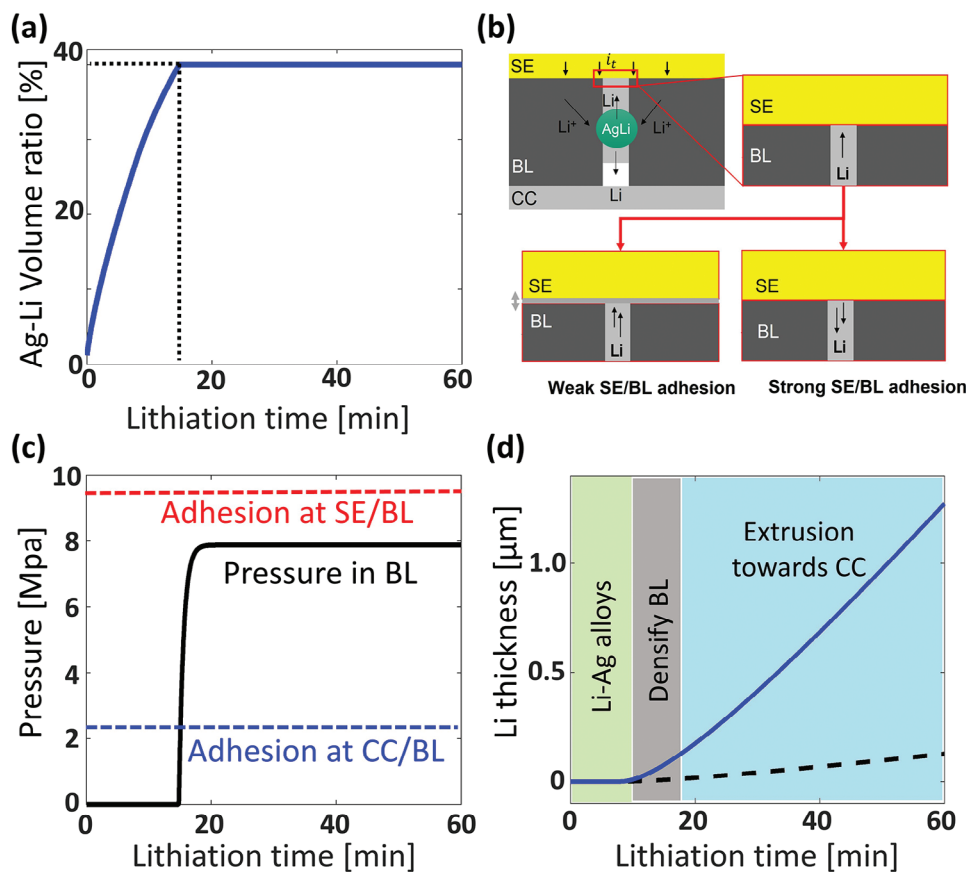


Figure 7. a) Volume percentage of Ag–Li alloy in the BL as a function of lithiation time, assuming the same experimental conditions as those in the work of Lee et al.^[21] The volume of Ag–Li alloy at varied compositions is estimated from the DFT computations in 2a. b) The mechanism for interface separation between the BL and SE. When the adhesion on the SE side is weaker than that on the CC side, the BL/SE interface separates first and the solid-solution extrudes toward the SE. When the adhesion on the SE side is stronger than that on the CC side, the BL/CC interface separates first and the solid-solution extrudes toward the CC. c) Calculated internal stress as a function of lithiation time in an anode-free setup using LLZO as the SE. d) Calculated evolution of deposited Li layer thickness as a function of the lithiation time on BL/SE and BL/CC interfaces combining electrochemical and mechanical effects.

of AgLi_y alloys are taken from the DFT computations. At a current density of 0.68 mA*cm⁻², Ag particles are expected to expand and entirely occupy the pores within the BL after ≈15 min. At this point, internal stress begins to accumulate, eventually causing separation at either the BL/SE or BL/CC interface. Figure 7c quantifies the evolution of internal hydro-static pressure in the BL with lithiation time, assuming that the adhesive strengths at both the SE/BL and CC/BL interfaces are substantial enough to preserve the interfacial bonding. Under this assumption, the internal pressure can reach a maximum of ≈8 MPa before Ag–Li alloying is restrained by an overpotential emerging from mechanical stress.^[7,50,62] In reality, interfacial adhesion is limited and heavily reliant on the properties of the contacting surfaces. Consequently, the interface with lower adhesion strength will be separated first, causing the Ag–Li solid solution to extrude toward that interface, resulting in an elastoplastic flow (Figure 7b). The BL/SE interface has been found to have stronger adhesion than the BL/CC interface,^[22,60] with respective values indicated by horizontal lines in Figure 7c. Once the internal stress is large enough to counterbalance the adhesion strength of the BL/CC interface (≈2 MPa) and the externally applied stack pressure

(≈1 MPa),^[21] the BL/CC interface will separate, relieving the internal stress and causing the Ag–Li alloy to extrude towards the CC.

Figure 7d combines both electrochemical factors (ASR) and mechanical factors (volume expansion, surface adhesion, plastic flow) to portray the evolution of the Li deposition thickness at the BL/CC and BL/SE interfaces with lithiation time. Ag particles are lithiated in the BL during the initial ≈10 min without significantly filling the BL pore volume. Over the next ≈8 min, the BL is densified as the Ag–Li alloy expands into the BL pores. During the subsequent ≈45 min, the Ag–Li solid solution mechanically extrudes toward the CC. This mechanism accounts for the predominant migration of Ag toward the CC after lithiation, as observed in scanning electron microscopy studies.^[21,22] Overall, the preference of Li metal to deposit on the BL/CC interface can be explained by the lower interfacial charge transfer resistance and the lower adhesion strength between the BL and CC compared to the BL and SE. The migration of Ag can be attributed to the elastoplastic flow of the Ag–Li solid solution resulting from the alloy’s volume expansion and extrusion toward the CC.

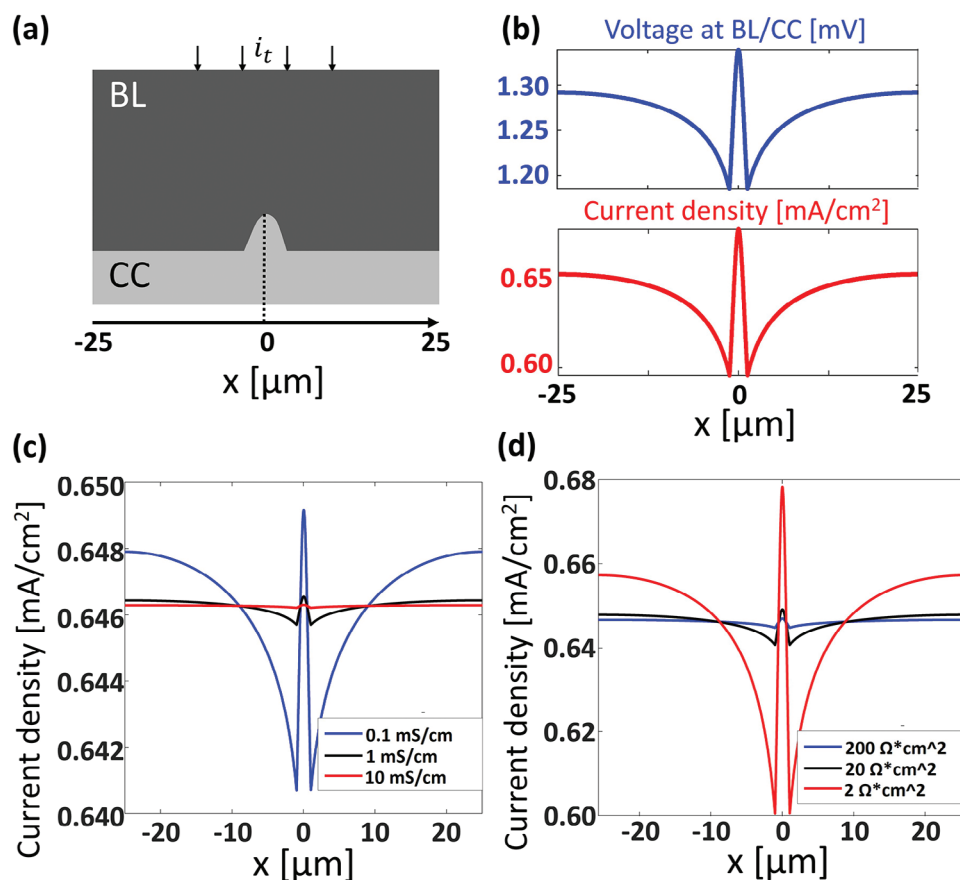


Figure 8. a) Schematics of a model interface between the BL and CC with a single $2\mu\text{m} \times 2\mu\text{m}$ tip defect on the CC. The x-axis measures the horizontal distance from the tip center. b) Simulated distribution of voltage (blue, upper panel) and Li current (red, lower panel) on the defected interface. The BL ionic conductivity is set to $1\text{ mS}\cdot\text{cm}^{-1}$ and the ASR is set to $2\Omega\cdot\text{cm}^2$. c) Simulated distribution of Li current on the defected interface at varied BL ionic conductivity: $0.1\text{ mS}\cdot\text{cm}^{-1}$ (blue), $1\text{ mS}\cdot\text{cm}^{-1}$ (black), and $10\text{ mS}\cdot\text{cm}^{-1}$ (red). The interfacial ASR is fixed to $2\Omega\cdot\text{cm}^2$. d) Simulated distribution of Li current on the defected interface at varied interfacial ASR: $200\Omega\cdot\text{cm}^2$ (blue), $20\Omega\cdot\text{cm}^2$ (black), and $2\Omega\cdot\text{cm}^2$ (red). The ionic conductivity of the BL is fixed to $0.1\text{ mS}\cdot\text{cm}^{-1}$.

2.3. Discussion

With a better understanding of the working mechanism of the Ag/C composite BL, we discuss the factors affecting the homogeneity of the Li current. When current concentration in typical intercalation or alloying electrode causes a local increase in lithiation, the local voltage decreases with respect to the rest of the electrode. This negative feedback mechanism reduces current concentration driving the electrode toward more homogeneous lithiation. Because the plating of metallic lithium occurs at constant voltage, no such negative feedback occurs, and a homogeneous current profile is fundamentally unstable leading to dendrite formation. To reduce the current instability one can either try to dampen the instability, or provide a negative feedback to any local excess Li deposition. Two examples of damping mechanisms, conductivity and ASR increase, are shown in Figure 8. Figure 8a schematically presents a defected interface between the BL and CC, featuring a single $2\mu\text{m} \times 2\mu\text{m}$ Gaussian-shaped Li-metal tip positioned on the CC. At a constant lithiation current ($i_t = 0.68\text{ mA}\cdot\text{cm}^{-2}$), Figure 8b shows the voltage (blue, upper panel) and Li current (red, lower panel) distribution on the interface. Indeed, as the tip protrudes into the BL it presents a higher

voltage (lower chemical potential) to the arriving lithium so that an excess Li plates at the tip. In our simulation, the $2\mu\text{m}$ wide tip attracts nearly 7% of the total current in the $50\mu\text{m}$ area around it, despite being only 4% of the line area. Improvement in the Li-ion conductivity of the BL can enhance the current homogeneity and reduce the speed at which dendrites grow. This behavior is displayed in Figure 8c, where the Li current becomes less concentrated at the tip as the BL ionic conductivity increases. This can be understood from the fact that a BL with high ionic conductivity (σ) effectively redirects current density (j) laterally to mitigate the voltage difference (ΔV) within a length l from the protruding defect tip, and can be qualitatively understood with the Ohmic relation $j = \frac{\sigma}{l} \Delta V$. For example, at a constant current of $1\text{ mA}\cdot\text{cm}^{-2}$, if the ionic conductivity is increased from 0.1 to $1\text{ mS}\cdot\text{cm}^{-1}$, the length scale over which the voltage drops by 1 mV will be increased from 1 to $10\mu\text{m}$.

Similarly, maintaining an appropriate ASR on the CC surface can also lead to more homogeneous Li plating. Figure 8d illustrates how a decrease in the ASR exacerbates the Li current inhomogeneity, thereby increasing the risk of dendrite formation. This can be easily understood since a high ASR essentially “backs up” current at the interface negating any voltage advantage of a

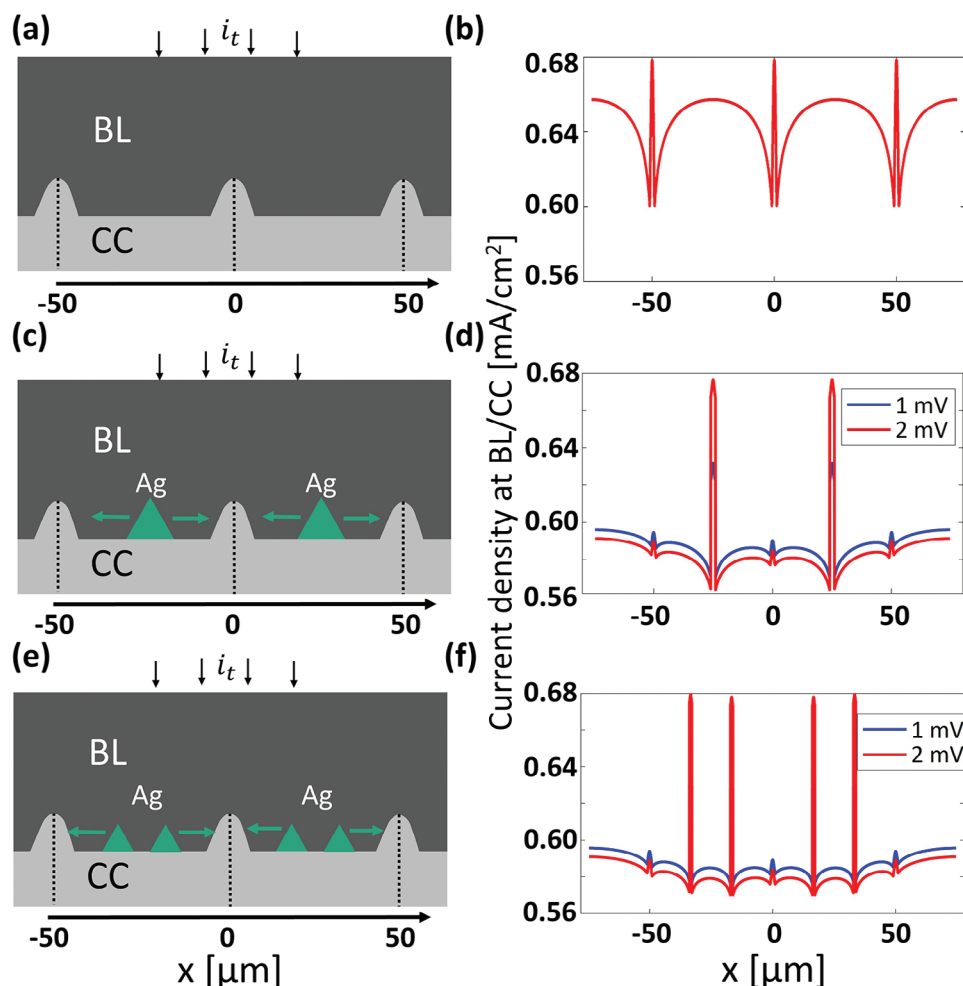


Figure 9. Effect of Ag particles on Li current distribution on a defective BL/CC interface. Simulations were performed imposing a constant average current $i_t=0.68 \text{ mA}\cdot\text{cm}^{-2}$ at the top surface. The BL ionic conductivity is fixed at $1 \text{ mS}\cdot\text{cm}^{-1}$ and the ASR is fixed at $2 \Omega\cdot\text{cm}^2$. a) Schematics of a BL/CC interface having three $2 \mu\text{m} \times 2 \mu\text{m}$ tip defects on the CC with a $50 \mu\text{m}$ distance between peaks. No Ag particles are included. The x -axis measures the horizontal distance from the central tip. b) Simulated current distribution on the x -axis by using the schematics described in (a). c) Schematics of a BL/CC with three tip defects, as described in (a), and two additional $2 \mu\text{m} \times 2 \mu\text{m}$ Ag particles at $x = -25 \mu\text{m}$ and $x = 25 \mu\text{m}$. d) Simulated current distribution on the x -axis for the geometry in (c). A lithiation driving force of 1 mV (blue) and 2 mV (red) is added to the regions where a Ag particle is present. e) Schematics of a BL/CC with three tip defects, as described in (a), and four additional $1 \mu\text{m} \times 1 \mu\text{m}$ Ag particles at $x = -33.3 \mu\text{m}$, $x = -16.7 \mu\text{m}$, $x = 16.7 \mu\text{m}$, and $x = 33.3 \mu\text{m}$. f) Simulated current distribution on the x -axis by using the schematics described in (e). A lithiation driving force of 1 mV (blue) and 2 mV (red) is added to the regions where a Ag particle is present.

dendrite tip. However, it is important to note that although a relatively raised ASR aids in suppressing dendrite growth, an excessively high ASR can result in high internal resistance, which is detrimental to the power density of the cell. Thus, an optimal interface design should account for the trade-off dictated by the interfacial ASR value. It should also be noted that the ASR that is varied in Figure 8d is the actual ASR of a BL/CC contact, unlike the macroscopically measured ASR that often reflects the presence of voids. An increase of ASR because of voids will actually lead to increased current inhomogeneity due to the reduction in contact.

While increases in the ASR or ionic conductivity dampen the current concentration caused by inhomogeneities, the presence of Ag as an alloying component of the electrode can contribute negative feedback to excess current in a particular area. We show

the influence that Ag particles on the current collector have on the current distribution in Figure 9c–f. To simplify the problem, we assume that Ag particles introduce a lithiation driving force of either 1 mV (blue) or 2 mV (red). This example is intended to understand the modification of the current distribution when even minor cathodic potential variations occur. In the absence of Ag particles (Figure 9a,b), the Li current concentrates at defect centers, as expected. However, with the introduction of a small amount of Ag nanoparticles between the tip defects (Figure 9c,d), the Li currents are redistributed from the defects and preferentially flow toward the Ag. Remarkably, even with only a 1 mV difference in local potential, the Ag is able to pull current away from the defect which is $25 \mu\text{m}$ away, illustrating the remarkable influence of small voltage variations on the anode, and pointing at the potential to artificially engineer Li deposition sites and homogeneity.

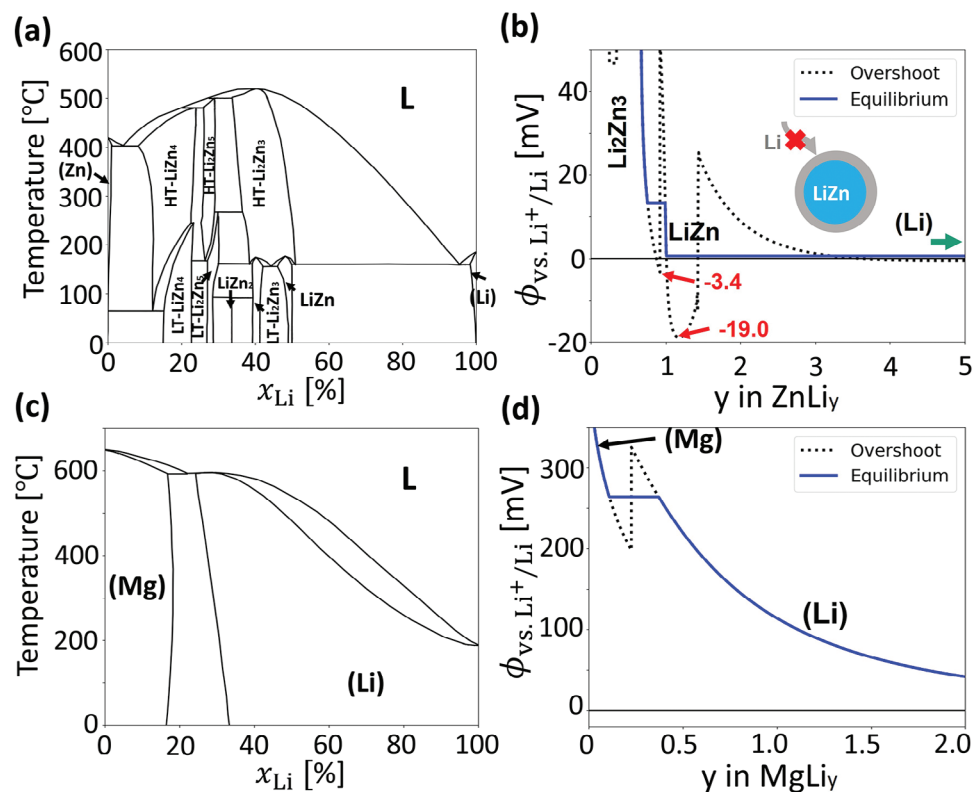


Figure 10. a) Composition–temperature phase diagram of the Zn–Li system, redrawn from Pelton.^[63] b) Lithiation potential of Zn as a function of y in formula $ZnLi_y$ at $T=300$ K, computed from a CALPHAD model. Both the equilibrium (blue solid) and over-saturation potentials (black dashed) are plotted. The sub-figure shows the Zn–Li alloy being unable to absorb more Li because of the negative overpotential. c) Composition–temperature phase diagram of the Mg–Li system reproduced from Nayeb et al.^[66] d) Lithiation potential of Mg as a function of y in the formula $MgLi_y$ at $T=300$ K computed from a CALPHAD model.^[67] Both the equilibrium potential (blue solid) and over-saturation potential (black dashed) are plotted.

When the total amount of Ag is kept constant, a larger amount of small Ag nanoparticles (Figure 9e,f) is more effective than fewer large particles, as more sites can be created to attract Li, thereby further preventing growth of the tip. As Ag particles lithiate and expand, the roughness on the CC surface can be filled, resulting in a more uniform surface for subsequent Li deposition. Hence, the benefits of Ag nanoparticles at the CC may arise from the creation of a homogeneous set of Li nucleation sites, unrelated to the interfacial unevenness, as well as from its ability to fill in surface roughness through its large volume expansion upon lithiation. Ag nanoparticles at the interface effectively hide the surface irregularities from the current.

We now turn our attention to the specific and rather unique role that the Ag–Li chemistry plays. The superior performance of Ag over other metals (Sn, Zn, Al, Ni, etc.) in the experiments of Lee et al.^[21] can be attributed to its ability to maintain an attractive driving force through the formation of a wide-ranging solid-solution. Figure 5d shows that even for $y = 25$ in $AgLi_y$, the alloying potential is above zero. Using the Zn–Li system as a comparative system, we illustrate the challenges in substituting Ag by other metals. Figure 10a presents the composition–temperature phase diagram of Zn–Li, reproduced from the work of Pelton.^[63] At room temperature, various compounds with narrow homogeneity ranges exist, including Li_2Zn_5 , $LiZn_2$, Li_2Zn_3 , and LiZn. A narrow phase field implies a rapid increase of free energy with

Li excess and, therefore, a sharp free-energy landscape. As shown in Figure 4c,d, compared to the α phase, the potential of the α' phase with a sharper free energy drops more rapidly as it is over-lithiated. Once the lithiation potential becomes negative, the alloy particle will cease to attract Li flow and redistribute Li currents, potentially causing dendrite formation. Figure 10b illustrates the non-equilibrium lithiation potential of Zn at $T = 300$ K computed from a CALPHAD model^[64] by Liang et al.^[65] The Zn–Li system exhibits significant negative overpotential across phases Li_2Zn_3 (-3.4 mV) and LiZn (-19.0 mV), suggesting that Zn is likely to stop lithiating prematurely and lose its attractiveness to Li unless two-phase nucleation can occur.

The inability of other metals to absorb enough Li (and hence be unable to expand sufficiently during lithiation) is the a reason why other metals do not perform, as well as Ag. Two important mechanisms are controlled by the maximum Li uptake in the metal. The more Li the metal takes up, the longer the current at the anode is controlled by the dispersion of the metal, rather than by geometric irregularities at the interface. Second, if a metal cannot densify pores in the BL after alloying with Li, it will not be able to extrude toward the CC and cannot precipitate on the CC after delithiation. Table 2 estimates the volume expansion ratio ($R = \text{Metal-Li molar volume/Pure metal molar volume}$) of various metals at ambient conditions from experimentally measured crystal structure and phase diagram data, under

Table 2. Ratio (R) of volume expansion in various metals at the maximum-Li-content phase, measured at room temperature and 1 atm. Molar volumes of the metal–Li alloys and the pure metal were computed from XRD data, as referenced. The data of Pt is marked with “?” as the phase PtLi₅ has not been confirmed.

Metal	Phase	Max x_{Li}	R	Refs.
Ag	γ_1	0.94	17.7	[33]
Au	Au ₄ Li ₁₅	0.789	4.7	[69]
Zn	ZnLi	0.5	2.0	[63]
Sn	Sn ₄ Li ₁₇	0.809	3.6	[70, 71]
Al	Al ₄ Li ₉	0.692	3.4	[72]
Cu	(Cu)	0.25	1.4	[73]
Ni	(Ni)	0	1	[74]
Si	Si ₄ Li ₁₇	0.809	4.1	[75, 76]
Bi	BiLi ₃	0.94	2.1	[77]
Pt(?)	PtLi ₅	0.833	6	[78]
Ga	GaLi ₂	0.667	2.4	[79]
Ge	Ge ₄ Li ₁₇	0.809	3.7	[71, 80]
Pb	Pb ₄ Li ₁₇	0.809	3.2	[71, 81]
Tl	Tl ₅ Li ₂₂	0.815	3.5	[82]
Sb	SbLi ₃	0.75	2.3	[83]
In	In ₃ Li ₁₃	0.812	4.0	[84]

the assumption that all metals can be maximally lithiated to their most Li-rich alloy phase. As argued in our example, for Zn–Li this may actually be an overestimation. Ag provides the largest volume expansion ratio ($R = 17.7$) compared to all other metals in the table, which mostly stop at $R < 4$. It is likely that Ag is the only metal capable of expanding sufficiently to extrude from the pores and deposit uniformly as nanoparticles on the CC surface after the first few cycles. Even accounting for the overpotential effects at practical current densities, Ag maintains a notable capacity for expansion compared to other metals. As illustrated in Figure 6b, at a current density of 0.68 mA*cm⁻², the electric potential of the Ag particle drops below 0V at around 8 mins, corresponding to approximately $y = 25$ in AgLi_y and thereby occupying roughly 20% of the buffer layer’s (BL’s) volume (Figure 7a). This behavior of Ag significantly contrasts with that of other metals, which cease to absorb Li at much lower Li contents. However, despite their inability to migrate during the pre-cycling like Ag, other metals could still be used to guide the Li current if their nanoparticles can be uniformly distributed on the CC during anode pre-processing. This has recently been evidenced by the study of Haslam et al. using Au nanoparticles as the nucleation sites.^[68] Achieving this requires understanding the specific characteristics of each metal and the corresponding processing methods when designing LMSSB systems.

Finally, our research suggests that Mg could also serve as a promising candidate for the BL. As illustrated by the Mg–Li phase diagram^[66] (Figure 10c), Mg and Li possess high intersolubility without the presence of any intermediate phase. Figure 10d indicates that the lithiation potential of Mg, computed from the model of Braga et al.,^[67] remains above 0 V. Therefore, Mg might operate via a solid-solution mechanism similar to that of Ag in the BL. Employing Mg in anode-free battery design could thus be a

promising future direction for research, though its high enthalpy of oxidation could make it challenging to use as a pure metal.

In summary, Figure 11 demonstrates the microscopic operating mechanism during the initial few charge–discharge cycles within an Ag/C BL. At the beginning of lithiation, the amorphous carbon within the BL rapidly saturates with Li and subsequently functions as an MIEC. The Ag particles then begin alloying with Li, forming a solid-solution phase. As lithiation continues, the Ag–Li alloy expands and separates the BL/CC interface under internal pressure, leading to extrusion towards the CC. Meanwhile, the remaining Ag and Ag-rich phases dissolve into the solid solution and plastically flow toward the CC. During delithiation, Li is extracted from the solid solution, resulting in the precipitation of Ag as uniformly distributed nanoparticles on the CC. These Ag nanoparticles help guide Li currents away from surface tips, suppressing surface coarsening and dendrite growth in subsequent cycles. Given the small nature of Ag nanoparticles left on the CC, it might need to be investigated in the future that the dispersion of Ag particle size does not coarsen when the battery is left in the delithiated state for a long time.

3. Conclusion

By integrating first-principles thermodynamic calculations and continuum modeling approaches, we have examined the lithiation and delithiation processes in Ag/C BL for an anode-free LMSSB. Our study identifies several key properties of the Ag–C buffer layer in creating homogeneous Li plating conditions. Computationally, we found that Ag can continuously alloy with and dissolve into Li, forming a solid-solution that consistently presents a positive attraction potential to Li, even at the AgLi₂₅ stage. This is unlike other metals for which equilibrium or non-equilibrium lithiation leads to negative potential at low Li content. This capability of Ag to absorb Li renders Ag nanoparticles as sinks to the Li flow, effectively homogenizing the current and mitigating the risk of Li-dendrite formation due to uncontrolled growth on surface defects. The large volume expansion is key to extrude the Ag–Li alloy from the pores, carrying Ag toward the CC where it is most effective in homogenizing the current. Our continuum modelling reveals that Li deposition is more favorable at the BL/CC interface than at the BL/SE interface, due to the lower interfacial resistance (ASR). The extrusion process predominantly occurs toward the CC due to the stronger surface adhesion between the SE and BL compared to that between the CC and BL. Our study also suggests that other metals may not perform well as they exhibit possible negative overpotentials due to near-stoichiometric compounds, cease to lithiate early, or lack the ability to sufficiently expand during lithiation.

4. Experimental Section

DFT Calculations: DFT calculations were performed within Vienna ab initio simulation package (VASP) using the projector-augmented wave method^[85,86] with a plane-wave basis set at an energy cutoff of 680 eV and a reciprocal space discretization of 800 k -points per Å. Ag 4p electrons were treated as valence electrons. All the calculations were converged to 10⁻⁵ eV in total energy for electronic loops and 0.01 eVÅ⁻¹ in inter-atomic forces for ionic loops. The calculations relied on the Perdew–Burke–Ernzerhof (PBE) generalized gradient approximation (GGA)^[87]

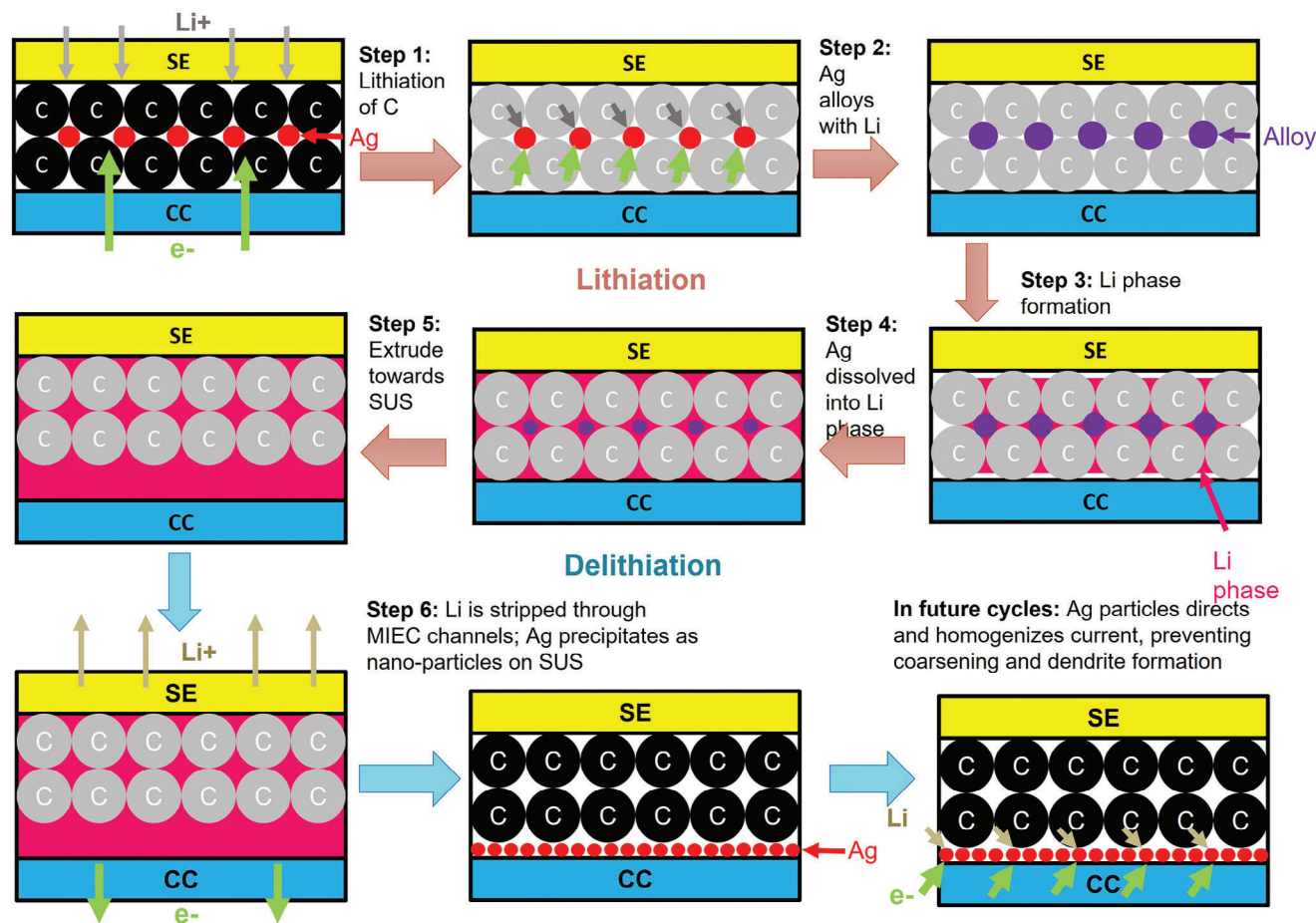


Figure 11. Proposed microscopic lithiation–delithiation mechanism of Ag/C BL during the first few cycles in the Ag/C BL. Amorphous carbon particles are shown as black and gray circles before and after saturating with Li, respectively Ag-metal particles are drawn as red circles. Ag-rich phases in the Ag–Li mixture are marked as purple circles while the Li-rich solid-solution is colored in pink.

exchange-correlation functional. Automated choice of parameters in structural relaxations and static calculations was performed using the Atomate^[88] and Fireworks^[89] packages.

Cluster Expansion and Free-Energy Calculations: The CE model for BCC-related phases (β -AgLi and Li solid-solution) was derived from a conventional BCC cubic cell with a lattice constant $a = 3.50 \text{ \AA}$ (Figure 12a). The CE model for the FCC Ag solid-solution phase was constructed using a conventional FCC cubic cell with $a = 4.27 \text{ \AA}$ (Figure 12b). The γ phase CE model was constructed from the γ -brass structure with $a = 9.62 \text{ \AA}$ with only B(OT) and C(OH) sites allowed to be occupied by Ag (Figure 12c). For the BCC lattice, configurations were enumerated within a diagonal supercell matrix defined by $((3, 0, 0)^T, (0, 3, 0)^T, (0, 0, 3)^T)$ and a non-diagonal supercell matrix given by $((-2, 2, 2)^T, (2, -2, 2)^T, (2, 2, -2)^T)$ to minimize the chance of having duplicated correlation functions between clusters. For the FCC phase, supercells $((4, 0, 0)^T, (0, 2, 0)^T, (0, 0, 2)^T)$ and $((3, 0, 0)^T, (1, 2, 0)^T, (0, 0, 2)^T)$ were used. For the γ phase, enumeration was performed within the original $1*1*1$ cubic cell. The cluster correlation functions were constructed from an indicator site basis.^[90] Among clusters with duplicate correlation functions in the feature matrix, only the shorter-ranged cluster was kept. A lasso regularization method^[91]

$$f(J) = \|E_{\text{DFT}} - \Pi J\|_2^2 + \alpha \|J\|_1 \quad (1)$$

was employed, where the l_1 -norm of effective interactions (ECIs, J) was incorporated to penalize the objective function ($f(J)$) during the fitting. This step is crucial for improving model sparsity and avoiding overfitting. The

regularization hyper-parameter (α) was fine-tuned using a grid-search approach to minimize the fivefold cross-validation error. The cluster cutoff diameters, count of cluster correlation functions, number of training structures, optimal α , root-mean-square errors (RMSE), and cross-validation errors (CV) from fitting are provided in Table 3. No quadruplet cluster could be included in the γ -phase CE within a cutoff of 4.5 \AA . Further details about the clusters and ECIs can be found in the Supporting Information.

The CE models, which function as effective Hamiltonians, were used to perform MC simulations in canonical ensembles at varying temperatures and compositions (x_{Li}). The simulations were executed within $8*6*6$, $6*6*4$ and $3*3*2$ supercells for BCC, FCC and γ lattices, respectively. The simulation temperature was gradually reduced (i.e., $T = 10000, 7000, 5000, 3000, 2000, 1500, 1200, 1000, 800, 700, 600, 500, 440, 400, 340, 300, 280, 260, 240, 220, 200, 180, 160, 140, 120, 100, 80, 60, 40, 20 \text{ K}$) to approach the configurational ground states at each x_{Li} and subsequently increased back to 500 K by steps. At each temperature higher or equal to 2000 K , $250,000$ metropolis steps were run. For temperatures between 500 and 2000 K , $500,000$ metropolis steps were used. For temperatures below or equal to 500 K , $1,000,000$ metropolis steps were used. The configurational contribution to free energy at each composition can be evaluated using

$$\beta F_c = \beta_0 E_0 + \int_{\beta_0}^{\beta} \langle E \rangle d\beta \quad (2)$$

where F_c is the configurational free energy at temperature T , $\beta = 1/k_B T$, k_B is the Boltzmann constant, $\langle E \rangle$ is the average energy computed at

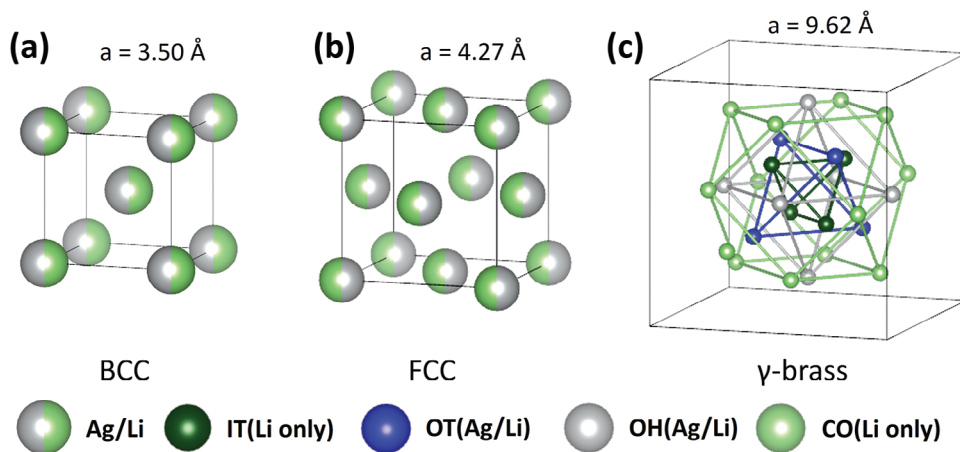


Figure 12. Primitive structures used for cluster expansions in the BCC, FCC, and the γ phase. Ag and Li are allowed to mix on all sites in BCC and FCC, whereas γ allows Ag to occur on OT(B) and OH(C) sites only. For visibility, only half of the sites in γ are shown. Other sites can be obtained by applying the $I43m$ symmetry.

temperature T , and E_0 is the average energy at a very low starting temperature T_0 corresponding to β_0 , where configurational entropy can be ignored. In this study, $T_0 = 20$ K is used, and integrated upward in T . Only the latter half of the metropolis steps at each temperature were used to compute the average energy to ensure that only the equilibrium distribution was sampled. All programming tools required for building the CE, fitting the ECLs and performing the MC simulations were available in the smol^[92] and sparse-lm^[93] packages.

Due to the computational challenges of running phonon calculations for all enumerated structures, and considering that the temperatures of interest are relatively low ($T \approx 300$ K), we computed the phonon free energy for only the end-point composition structures in each lattice ($x_{\text{Li}} = 0, 1$ for BCC and FCC, $x_{\text{Li}} = 8/13, 1$ for γ) and several ordered ground-state structures at intermediate compositions. Using the quasi-harmonic approximation implemented in Phonopy,^[94,95] the vibrational frequencies and phonon free energy at $T = 0-10000$ K were calculated from a supercell of each structure with a lattice constant $a \approx 10$ Å. We linearly interpolated the vibrational free energy (F_{vib}) of structures over x_{Li} on each lattice and added the interpolated free energies as correction terms to the total free energy (see Supporting information).

The total free energy (F^i) of each phase ($i = \text{BCC, FCC and } \gamma$) was represented as a function of composition (x) and temperature (T)

$$F^i(x, T) = F_c^i(x, T) + F_{\text{vib}}^i(x, T) \quad (3)$$

and the formation free energy (ΔF^i) was computed using the free energy of BCC Li ($F^{\text{BCC}}(x = 1, T)$) and FCC Ag ($F^{\text{FCC}}(x = 0, T)$) at the same temperature T as references

$$\Delta F^i(x, T) = F^i(x, T) - xF^{\text{BCC}}(x = 1, T) - (1-x)F^{\text{FCC}}(x = 0, T) \quad (4)$$

Table 3. Detailed information of CE models, including cluster cutoff diameters, number of fitted clusters (N_c), number of training structures (N_s), RMSE and CV for BCC, FCC, and γ .

Model	Cluster cutoffs [Å]	N_c	N_s	α	RMSE [meV*at. ⁻¹]	CV [meV*at. ⁻¹]
BCC	8.0(pair); 7.0(triplet); 4.5(quadruplet)	25	64	3.8×10^{-6}	3.3	4.8
FCC	8.0(pair); 7.0(triplet); 4.5(quadruplet)	32	134	9.5×10^{-7}	1.5	2.5
γ	8.0(pair); 7.0(triplet)	38	96	6.1×10^{-5}	0.5	0.6

The equilibrium lithiation potential in each phase (ϕ^i) at temperature T can be calculated as

$$e\phi^i(x, T) = F^{\text{BCC}}(x = 1, T) - F^i(x, T) - (1-x)\frac{\partial F^i}{\partial x} \quad (5)$$

where e is the elementary charge.

Mixed Ionic-Electronic Conduction in the Ag/C BL: The transport of Li^+ and electron in the BL using the Ohmic relations is described

$$i_{\text{Li}^+} = -\frac{\sigma_{\text{Li}^+}}{F} \nabla \tilde{\mu}_{\text{Li}^+}, \quad i_{e^-} = \frac{\sigma_{e^-}}{F} \nabla \tilde{\mu}_{e^-} \quad (6)$$

In these equations, i_{Li^+} and i_{e^-} represent the current density of Li ion and electron in the BL, respectively. The symbols σ_{Li^+} and σ_{e^-} denote the Li-ion and electronic conductivity of the BL, respectively. Additionally, $\tilde{\mu}_{\text{Li}^+}$ and $\tilde{\mu}_{e^-}$ are the electrochemical potentials of Li^+ and electron, respectively. The sum of these two electrochemical potentials were required to be equal to the chemical potential of Li in the BL ($\tilde{\mu}_{\text{Li}^+} + \tilde{\mu}_{e^-} = \mu_{\text{Li}}$). The concentration of Li^+ in the BL can be further characterized by employing both the Ohmic relations and the Nerst-Planck equation, as shown below:

$$\frac{\partial C_{\text{Li}^+}}{\partial t} = -D_{\text{Li}^+} \nabla^2 C_{\text{Li}^+} - \sigma_{\text{Li}^+} \nabla^2 \tilde{\mu}_{\text{Li}^+} \quad (7)$$

In this equation, D_{Li^+} represents the diffusivity of Li ions in the BL.

Charge-Transfer Kinetics for Li Deposition at the Interfaces: The lithiation rate at the interfaces could be represented by the current density of Li^+ participating in the redox reaction. As proposed by Ganser et al.,^[96] the Butler-Volmer equation provided below reflects the relationship between the interface overpotential (η) and the lithiation current (i_n).

$$i_n = -i_{\text{ex}} e^{\frac{(1-\alpha_a)\tilde{V}_{\text{Li}}\Delta P}{RT}} \left(e^{\frac{\alpha_a F}{RT} \eta} - e^{-\frac{\alpha_c F}{RT} \eta} \right) \quad (8)$$

In the Butler-Volmer equation, i_n represents the local current density normal to the interface and i_{ex} is the reference exchange current density for the Li^+/Li redox reaction. The parameters α_a and α_c denote the anodic and cathodic charge-transfer coefficients, respectively, whereas \bar{V}_{Li} is the molar volume of the Ag–Li alloy (estimated with that of Li metal). R refers to the ideal gas constant, and F is the Faraday constant. In order to account for the effect of mechanical stress on Li deposition, we performed a mechanical correction to the interface overpotential, as shown below:

$$\eta = \phi - \phi_{\text{BL}} - \phi_0 - \frac{\bar{V}_{\text{Li}} \Delta P}{F} \quad (9)$$

here, ϕ denotes the electric potential at the interface, ϕ_{BL} represents the electric potential in the BL, and ϕ_0 is the equilibrium open-circuit potential without external stress. The symbol ΔP denotes the compressive stress within the BL.

Modelling Mechanical Stress Within the BL: To simulate the development of compressive stress within the BL, assuming that mechanical equilibrium could be achieved in a much shorter time than chemical equilibrium.^[97] Therefore, a quasi-static mechanical equilibrium could always be maintained within the BL. This equilibrium using the following linear-momentum balance constraint is enforced:

$$\nabla \cdot \sigma = 0 \quad (10)$$

In this equation, σ symbolizes the second-order stress tensor that must have a zero divergence. The stress tensor can further be decomposed into a deviatoric and hydrostatic component as:

$$\sigma = -PI + s \quad (11)$$

here, P represents the hydrostatic pressure ($P = -\frac{1}{3}\text{Tr}(\sigma)$) with positive and negative values indicating compression and expansion states, respectively.

The evolution of mechanical stress is derived within the BL as follows:

$$\begin{aligned} dP/dt &= \frac{K\bar{V}_{\text{Li}}}{VF} I \\ I &= \oint i_n dS \end{aligned} \quad (12)$$

In these equations, V indicates the volume of the alloy particle, K represents the bulk modulus of the alloy (estimated similarly to that of Li metal), and I denotes the total lithiation current integrated across the Ag–Li particle surface. After substituting Equations (8) and (9) into Equation (12) and solving the resulting differential equation, the following relationship is obtained, which was used to compute the stress evolution displayed in Figure 7c:

$$\begin{aligned} P &= \frac{\oint F\eta dS}{\bar{V}_{\text{Li}} S} (1 - e^{-\gamma t}) \\ \gamma &= \frac{K\bar{V}_{\text{Li}}^2 S}{RTFV} i_{\text{ex}} \end{aligned} \quad (13)$$

Note that in these equations, the starting time ($t = 0$) corresponds to the moment when the pores in the BL were entirely filled, which occurred at approximately 15 min in Figure 7c.

Supporting Information

Supporting Information is available from the Wiley Online Library or from the author.

Acknowledgements

F.X. and Q.H.T. contributed equally to this work. This work was funded by the U.S. Department of Energy (DOE), Office of Science, Office of Basic Energy Sciences, Materials Sciences and Engineering Division under Contract No. DE-AC0205CH11231 (Materials Project program, KC23MP), and the Assistant Secretary for Energy Efficiency and Renewable Energy (EERE), Vehicle Technologies Office, under the Advanced Battery Materials Research (BMR) Program of the U.S. Department of Energy under Contract No. DE-AC02-05CH11231. The work was also supported with the computational resources provided by the National Energy Research Scientific Computing Center (NERSC), a U.S. Department of Energy Office of Science User Facility located at Lawrence Berkeley National Laboratory, the computational resources sponsored by the DOE Office of Energy Efficiency and Renewable Energy (EERE) and located at the National Renewable Energy Laboratory (NREL), and the Lawrence Livermore National Laboratory. The authors thank Dr. Nathalie Dupin for helpful discussions on CALPHAD models. The authors also gratefully acknowledged Dr. Srinath Chakravarthy from Factorial Energy, Dr. Eric Yang Wang from Samsung Advanced Institute of Technology, and Dr. Lincoln Miara from Pure Lithium, for insightful discussions on the modeling and experiments of the anode-free solid-state system.

Conflict of Interest

The authors declare no conflict of interest.

Data Availability Statement

The data that support the findings of this study are available from the corresponding author upon reasonable request.

Keywords

Ag/C buffer layer, anode free, continuum modelling, first-principles thermodynamics, lithium-metal solid-state battery (LMSSB)

Received: September 4, 2023

Revised: November 1, 2023

Published online: February 1, 2024

- [1] Y. Tian, G. Zeng, A. Rutt, T. Shi, H. Kim, J. Wang, J. Koettgen, Y. Sun, B. Ouyang, T. Chen, Z. Lun, Z. Rong, K. Persson, G. Ceder, *Chem. Rev.* **2020**, *121*, 1623.
- [2] Q. Zhang, D. Cao, Y. Ma, A. Natan, P. Aurora, H. Zhu, *Adv. Mater.* **2019**, *31*, 1901131.
- [3] K. Yoon, S. Lee, K. Oh, K. Kang, *Adv. Mater.* **2022**, *34*, 2104666.
- [4] Y. Xiao, Y. Wang, B. Shou-Hang, J. C. Kim, G. Ceder, *Nat. Rev. Mater.* **2021**, *6*, 868.
- [5] P. Albertus, S. Babinec, S. Litzelman, A. Newman, *Nat. Energy* **2018**, *3*, 16.
- [6] W. Luo, Y. Gong, Y. Zhu, Y. Li, Y. Yao, Y. Zhang, K. Fu, G. Pastel, C.-F. Lin, Y. Mo, E. D. Wachsman, L. Hu, *Adv. Mater.* **2017**, *29*, 1606042.
- [7] Q. Tu, L. Barroso-Luque, T. Shi, G. Ceder, *Cell Rep. Phys. Sci.* **2020**, *1*, 100106.
- [8] S. Kim, C. Jung, H. Kim, K. E. Thomas-Alyea, G. Yoon, B. Kim, M. E. Badding, Z. Song, J. Chang, J. Kim, D. Im, K. Kang, *Adv. Energy Mater.* **2020**, *10*, 1903993.
- [9] Y. Lu, C.-Z. Zhao, H. Yuan, X.-B. Cheng, J.-Q. Huang, Q. Zhang, *Adv. Funct. Mater.* **2021**, *31*, 2009925.

- [10] H. Wang, H. Gao, X. Chen, J. Zhu, W. Li, Z. Gong, Y. Li, M.-S. Wang, Y. Yang, *Adv. Energy Mater.* **2021**, *11*, 2102148.
- [11] P. Barai, A. T. Ngo, B. Narayanan, K. Higa, L. A. Curtiss, V. Srinivasan, *J. Electrochem. Soc.* **2020**, *167*, 100537.
- [12] F. Han, A. S. Westover, J. Yue, X. Fan, F. Wang, M. Chi, D. N. Leonard, N. J. Dudney, H. Wang, C. Wang, *Nat. Energy* **2019**, *4*, 187.
- [13] X. Liu, R. Garcia-Mendez, A. R. Lupini, Y. Cheng, Z. D. Hood, F. Han, A. Sharafi, J. C. Idrobo, N. J. Dudney, C. Wang, C. Ma, J. Sakamoto, M. Chi, *Nat. Mater.* **2021**, *20*, 1485.
- [14] J. Lau, R. H. DeBlock, D. M. Butts, D. S. Ashby, C. S. Choi, B. S. Dunn, *Adv. Energy Mater.* **2018**, *8*, 1800933.
- [15] E. Kazyak, R. Garcia-Mendez, W. S. LePage, A. Sharafi, A. L. Davis, A. J. Sanchez, K.-H. Chen, C. Haslam, J. Sakamoto, N. P. Dasgupta, *Matter* **2020**, *2*, 1025.
- [16] Y.-W. Byeon, H. Kim, *Electrochem* **2021**, *2*, 452.
- [17] M. Otoyama, M. Suyama, C. Hotehama, H. Kowada, Y. Takeda, K. Ito, A. Sakuda, M. Tatsumisago, A. Hayashi, *ACS Appl. Mater. Interfaces* **2021**, *13*, 5000.
- [18] J. Kasemchainan, S. Zekoll, D. Spencer Jolly, Z. Ning, G. O. Hartley, J. Marrow, P. G. Bruce, *Nat. Mater.* **2019**, *18*, 1105.
- [19] M. J. Wang, R. Choudhury, J. Sakamoto, *Joule* **2019**, *3*, 2165.
- [20] M. Wang, J. B. Wolfenstine, J. Sakamoto, *Electrochim. Acta* **2019**, *296*, 842.
- [21] Y.-G. Lee, S. Fujiki, C. Jung, N. Suzuki, N. Yashiro, R. Omoda, D.-S. Ko, T. Shiratsuchi, T. Sugimoto, S. Ryu, J. H. Ku, T. Watanabe, Y. Park, Y. Aihara, D. Im, I. T. Han, *Nat. Energy* **2020**, *5*, 299.
- [22] N. Suzuki, N. Yashiro, S. Fujiki, R. Omoda, T. Shiratsuchi, T. Watanabe, Y. Aihara, *Adv. Energy Sustainability Res.* **2021**, *2*, 2100066.
- [23] J.-S. Kim, G. Yoon, S. Kim, S. Sugata, N. Yashiro, S. Suzuki, M.-J. Lee, R. Kim, M. Badding, Z. Song, J. Chang, D. Im, *Nat. Commun.* **2023**, *14*, 782.
- [24] S. H. Park, D. Jun, J. E. Jung, S. G. Lee, G. H. Lee, Y. J. Lee, *J. Mater. Chem. A* **2022**, *10*, 21995.
- [25] S. Kim, G. Yoon, S.-K. Jung, S. Park, J.-S. Kim, K. Yoon, S. Lee, K. Kang, *ACS Energy Lett.* **2022**, *8*, 9.
- [26] D. Spencer-Jolly, V. Agarwal, C. Doerrer, B. Hu, S. Zhang, D. L. Melvin, H. Gao, X. Gao, P. Adamson, O. V. Magdysyuk, P. S. Grant, R. A. House, P. G. Bruce, *Joule* **2023**, *7*, 503.
- [27] S. Pastorello, *Gazz. Chim. Ital.* **1930**, *60*, 493.
- [28] S. Pastorello, *Gazz. Chim. Ital.* **1931**, *61*, 47.
- [29] W. Freeth, G. Raynor, *J. Inst. Metals* **1954**, *82*, 1556.
- [30] H. Perltz, *Zeitschrift für Kristallogr.-Cryst. Mater.* **1933**, *86*, 155.
- [31] L. Arnberg, S. Westman, *Acta Chemica Scandinavica* **1972**, *26*, 513.
- [32] T. Noritake, M. Aoki, S. i. Towata, T. Takeuchi, U. Mizutani, *Acta Crystallogr., Sect. B: Struct. Sci.* **2007**, *63*, 726.
- [33] A. Pelton, *Bull. Alloy Phase Diagrams* **1986**, *7*, 223.
- [34] M. Braga, A. Dębski, S. Terlicka, W. Gąsior, A. Góral, *J. Alloys Compd.* **2020**, *817*, 152811.
- [35] A. Zunger, S.-H. Wei, L. Ferreira, J. E. Bernard, *Phys. Rev. Lett.* **1990**, *65*, 353.
- [36] A. Seko, Y. Koyama, I. Tanaka, *Phys. Rev. B* **2009**, *80*, 165122.
- [37] A. J. Bradley, J. Thewlis, *Proc. Royal Soc. London. Series A* **1926**, *112*, 678.
- [38] U. Mizutani, R. Asahi, H. Sato, T. Noritake, T. Takeuchi, *J. Phys.: Condens. Matter* **2008**, *20*, 275228.
- [39] A. Jain, S. P. Ong, G. Hautier, W. Chen, W. D. Richards, S. Dacek, S. Cholia, D. Gunter, D. Skinner, G. Ceder, K. A. Persson, *APL Mater.* **2013**, *1*, 011002.
- [40] G. Bergerhoff, I. Brown, F. Allen, *Int. Union Crystallogr., Chester* **1987**, *360*, 77.
- [41] A. Bradley, C. Gregory, *Lond. Edinb. Dublin philos. mag. j. sci.* **1931**, *12*, 143.
- [42] W. Sven, N. Stina, S. Berndt, M. Olof, H. Merv, *Acta Chem. Scand.* **1965**, *19*, 1411.
- [43] M. A. Rollier, E. Arreghini, *Zeitschrift für Kristallogr.-Cryst. Mater.* **1939**, *101*, 470.
- [44] W. Obrowski, *Metallwissenschaft und Technik* **1963**, *17*, 108.
- [45] A. Johansson, H. Ljung, S. Westman, *Acta Chem. Scand.* **1968**, *22*, 2743.
- [46] L. Gulay, J. Schuster, *J. Alloys Compd.* **2003**, *360*, 137.
- [47] J. M. Sanchez, F. Ducastelle, D. Gratias, *Phys. A: Stat. Mech. Appl.* **1984**, *128*, 334.
- [48] G. Ceder, *Comput. Mater. Sci.* **1993**, *1*, 144.
- [49] A. van de Walle, G. Ceder, *J. Phase Equilib.* **2002**, *23*, 348.
- [50] Q. Tu, T. Shi, G. Ceder, in *Electrochemical Society Meeting Abstracts prime2020*, 5, The Electrochemical Society, Inc., Pennington, NJ, USA **2020**, pp. 972–972.
- [51] B. Orvananos, H.-C. Yu, A. Abdellahi, R. Malik, C. P. Grey, G. Ceder, K. Thornton, *J. Electrochem. Soc.* **2015**, *162*, A965.
- [52] S. Narayan, L. Anand, *Extreme Mech. Lett.* **2018**, *24*, 21.
- [53] J. N. Reddy, *Introduction to the finite element method*, McGraw-Hill Education, New York City **2019**.
- [54] R. Malik, F. Zhou, G. Ceder, *Nat. Mater.* **2011**, *10*, 587.
- [55] J. C. Bachman, S. Mui, A. Grimaud, H.-H. Chang, N. Pour, S. F. Lux, O. Paschos, F. Maglia, S. Lupart, P. Lamp, L. Giordano, Y. Shao-Horn, *Chem. Rev.* **2016**, *116*, 140.
- [56] K. Persson, V. A. Sethuraman, L. J. Hardwick, Y. Hinuma, Y. S. Meng, A. Van Der Ven, V. Srinivasan, R. Kostecki, G. Ceder, *J. Phys. Chem. Lett.* **2010**, *1*, 1176.
- [57] H. Tachikawa, A. Shimizu, *J. Phys. Chem. B* **2006**, *110*, 20445.
- [58] J. H. Park, H. Yoon, Y. Cho, C.-Y. Yoo, *Materials* **2021**, *14*, 4683.
- [59] M. Morgan, *Thin Solid Films* **1971**, *7*, 313.
- [60] M. Wang, J. Sakamoto, *J. Power Sources* **2018**, *377*, 7.
- [61] K. Yan, Z. Lu, H.-W. Lee, F. Xiong, P.-C. Hsu, Y. Li, J. Zhao, S. Chu, Y. Cui, *Nat. Energy* **2016**, *1*, 1.
- [62] R. Akolkar, *J. Power Sources* **2013**, *232*, 23.
- [63] A. Pelton, *J. Phase Equilib.* **1991**, *12*, 42.
- [64] N. Saunders, A. P. Miodownik, *CALPHAD (calculation of phase diagrams): a comprehensive guide*, Elsevier, Amsterdam **1998**.
- [65] Y. Liang, Z. Du, C. Guo, C. Li, *J. Alloys Compd.* **2008**, *455*, 236.
- [66] A. Nayeb-Hashemi, J. Clark, A. Pelton, *Bull. Alloy Phase Diagrams* **1984**, *5*, 365.
- [67] M. Braga, L. Malheiros, M. Härmäläinen, *Thermochim. Acta* **2000**, *344*, 47.
- [68] C. Haslam, J. Sakamoto, *J. Electrochem. Soc.* **2023**, *170*, 040524.
- [69] A. Pelton, *Bull. Alloy Phase Diagrams* **1986**, *7*, 228.
- [70] J. Sangster, C. Bale, *J. Phase Equilib.* **1998**, *19*, 70.
- [71] G. Goward, N. Taylor, D. Souza, L. Nazar, *J. Alloys Compd.* **2001**, *329*, 82.
- [72] A. McAlister, *Bull. Alloy Phase Diagrams* **1982**, *3*, 177.
- [73] A. Pelton, *Bull. Alloy Phase Diagrams* **1986**, *7*, 142.
- [74] H. Leavenworth, R. Cleary, *Acta. Met.* **1961**, *9*.
- [75] H. Okamoto, *Bull. Alloy Phase Diagrams* **1990**, *11*, 306.
- [76] M. Zeilinger, D. Benson, U. Haussermann, T. F. Fässler, *Chem. Mater.* **2013**, *25*, 1960.
- [77] J. Sangster, A. Pelton, *J. Phase Equilib.* **1991**, *12*, 447.
- [78] J. Sangster, A. Pelton, *J. Phase Equilib.* **1991**, *12*, 678.
- [79] J. Sangster, A. Pelton, *J. Phase Equilib.* **1991**, *12*, 33.
- [80] J. Sangster, A. Pelton, *J. Phase Equilib.* **1997**, *18*, 289.
- [81] H. Okamoto, *J. Phase Equilib.* **1993**, *14*, 770.
- [82] J. Sangster, *J. Phase Equilib. Diffus.* **2018**, *39*, 74.
- [83] J. Sangster, A. Pelton, *J. Phase Equilib.* **1993**, *14*, 514.
- [84] J. Sangster, A. Pelton, *J. Phase Equilib.* **1991**, *12*, 37.
- [85] G. Kresse, J. Furthmüller, *Phys. Rev. B* **1996**, *54*, 169.
- [86] G. Kresse, D. Joubert, *Phys. Rev. B* **1999**, *59*, 1758.
- [87] J. P. Perdew, K. Burke, Y. Wang, *Phys. Rev. B* **1996**, *54*, 16533.
- [88] K. Mathew, J. H. Montoya, A. Faghaninia, S. Dwarakanath, M. Aykol, H. Tang, I.-h. Chu, T. Smidt, B. Bocklund, M. Horton, J. Dagdelen, B.

- Wood, Z.-K. Liu, J. Neaton, S. P. Ong, K. Persson, A. Jain, *Comput. Mater. Sci.* **2017**, 139, 140.
- [89] A. Jain, S. P. Ong, W. Chen, B. Medasani, X. Qu, M. Kocher, M. Brafman, G. Petretto, G.-M. Rignanese, G. Hautier, D. Gunter, K. A. Persson, *Concurr. Comput. Pract. Exp.* **2015**, 27, 5037.
- [90] L. Barroso-Luque, P. Zhong, J. H. Yang, F. Xie, T. Chen, B. Ouyang, G. Ceder, *Phys. Rev. B* **2022**, 106, 144202.
- [91] L. J. Nelson, G. L. Hart, F. Zhou, V. Ozoliņš, *Phys. Rev. B* **2013**, 87, 035125.
- [92] L. Barroso-Luque, J. H. Yang, F. Xie, T. Chen, R. L. Kam, Z. Jadidi, P. Zhong, G. Ceder, *J. Open Source Softw.* **2022**, 7, 4504.
- [93] L. Barroso-Luque, Sparse linear regression models, <https://pypi.org/project/sparse-lm/>, (accessed: December 2022).
- [94] A. Togo, I. Tanaka, *Scr. Mater.* **2015**, 108, 1.
- [95] A. Togo, *J. Phys. Soc. Jpn.* **2023**, 92, 012001.
- [96] M. Ganser, F. E. Hildebrand, M. Klinsmann, M. Hanauer, M. Kamlah, R. M. McMeeking, *J. Electrochem. Soc.* **2019**, 166, H167.
- [97] X. Zhang, W. Shyy, A. M. Sastry, *J. Electrochem. Soc.* **2007**, 154, A910.